Investigation of the radial bearing force developed during actual ship operations. Part 2: Unsteady maneuvers

Fabrizio Ortolani[a], Salvatore Mauro[a], Giulio Dubbioso[a,*]

[a] *CNR-INSEAN, via di Vallerano 139, 00128 Roma, Italy*

Abstract

The bearing radial load developed by a propeller during actual ship operating conditions is deeply investigated by means of a free running, self propelled twin screw model at the CNR–INSEAN outdoor maneuvering model basin. The present work further extends to transient maneuvers the results discussed in *PartI* (Ortolani et al., xxx), focused on the quasi–steady conditions (straight ahead motion and steady turning). After the rudder actuation (both at the start of the turning circle and the pull–out phase), peaks 100% higher than the stabilized value were highlighted, in particular on the internal shaft. To deeply inspect this aspect, the inertial contribution of the propeller mass is reconstructed by the measurement of the 6DoF motion of the model and is removed from the measured force in order to obtain the hydrodynamic force exerted by the propeller. In addition to the turning circles, $\pm 10°$–$\mp 10°$, $\pm 20°$–$\mp 20°$and $\pm 35°$–$\mp 35°$zig–zag maneuvers at three different speeds ($F_N = 0.26, 0.32, 0.36$) were carried out in order to perform an extended investigation of the transient behavior of the propulsion system. The paper is presented following the same phenomenological perspective adopted in the previous work in order to clarify the nature of the bearing radial force during transient phases.

Keywords: Bearing radial force, Off–design propeller performance, transient loads, ship maneuvering, propeller–wake interaction

*Corresponding author.
Email address: `giudubbioso@libero.it` (Giulio Dubbioso)

1. Introduction

The prediction of the propeller performance in hull behind conditions during actual ship operations represents a crucial task since the early design stages. In fact, the propeller is the primary source of vibrations, caused by hub loads and the pulsating pressure field generated by the blades, and noise, its regime being intrinsically unsteady as a consequence of the complicated 3–D character of the wake field induced by upstream presence of the hull. In particular, the transverse (in–plane) components of the wake cause the propeller to generate in–plane forces and moments in addition to the propulsive loads (thrust and torque), i.e. the bearing loads. The quantification of these components is a primary goal to safely design the shafting of a ship in order to guarantee the continuity of operation at sea and, moreover, to optimize the structural layout of the hull. During the actual operation at sea, the propeller may experience inflow conditions that might be completely different from the reference one that is usually considered at the preliminary design stages (namely the one resulting in straight ahead sailing at the target speed/speeds) because of the wave induced motions or tight maneuvering (i.e., off–design conditions).

In these circumstances, in fact, the variation of the inflow conditions is responsible of a large increase of thrust and torque generated by the propeller, as pointed out by the experimental results performed both at full and model scale on twin screws (Coraddu et al., 2013). Moreover, the bearings may be critically overstressed, because the presence of larger in–plane velocities (induced both by the motion and the modification of the wake) might cause the increase of the radial force.

On these basis, the quantification of the radial load exerted by the propeller on the bearings during both design and off–design conditions, is a necessary task to develop and improve modern ship design methodologies in order to guarantee safety and continuity of ship operation at sea.

To bridge this gap, an extensive experimental champaign was carried at the outdoor CNR–INSEAN maneouvering basin on an unmanned, self–propelled, free running manoeuvering model of an high speed twin screw vessel. A partial presentation of the results focused on quasi–steady ship operational conditions (namely, straight ahead sailing and stabilized phase of the turning circle)was extensively described in Part I (Ortolani et al., xxx).

The phenomenon was deeply inspected in a cause–and–effect fashion by inferring a strict relationship between the morphology of the propeller inflow with the attitude of the model. In particular, it was highlighted that the bearing radial force experiences a marked variation (both in magnitude and orientation) moving from the straight to the steady phase of the turns. This behavior was ascribed to the character of the wake experienced during these conditions. In particular, during straight motion, the radial force is mainly directed up–wards (consistently to a propeller inflow characterized by a vertical component considerably larger than the horizontal one) and it amounts to 10–15% of the propeller thrust. On the contrary, the behavior during the turning phase was considerably different depending on the position of the shaft with respect to the center of the turn: on the external side (i.e., windward), the radial force is mainly directed horizontally and increases with rudder angle up to a value doubled with respect to the approach phase, whereas on the leeward side, the radial force evidenced a non–linear behavior with rudder angle, the horizontal component progressively increasing with respect to the vertical one. In both cases, the radial force is oriented such to stabilize the vessel i.e., the turning qualities are worsened. These results confirmed the trend investigated experimentally during turning motions on captive model tests on a similar twin screw model (Atsavapranee et al., 2010) and the measurements carried out at full scale on different kind of vessels (single and twin screw) (Gurr and Rulfs, 2008; Vartdal et al., 2009).

It has to be stressed that the use of a free running model allowed to further inspect the propeller behavior during transients, the dynamic response of the model being reproduced as closer as possible (for less than the scale effects) to actual conditions. During transient regimes, in fact, the propeller can generate loads 100% higher than those generated during the same, but steady, conditions because of dynamic inflow effects caused by the time history of the shedding of vorticity past the wake (i.e., a "memory effect") (Amini and Steen, 2012).

The free running model tests evidenced that, immediately after the actuation of the rudder (start of the maneuver and pull–out phases), peaks greater by almost 100% that occurring during the steady phase of the turn were experienced by the strut bearing; the phenomenology during transient was addressed, only qualitatively in Part I, to both damping and inertial effects induced the motion of the model in the transverse plane (coupled sway–roll).

Present work is principally aimed to gain a deeper insight on the phenomenology occurring during the transient phases. The transient phases of the turning circle (after the actuation of the rudder and pull–out) and zig–zag maneuvers are systematically investigated by a quantitative cross–correlation of the dynamic response of the model and the vertical and horizontal components of the radial force. A 35°–35°zig–zag maneuver was further performed in addition to the standard ones (20°–20°and 10°–10°) in order to tackle the phenomenology occurring during the transient response at large drift angles; the tests were carried out at three different speeds, namely $F_N = 0.26, 0.32$ and 0.35.

The results will be discussed following the same phenomenological style and the cause–and–effect approach proposed in Part I (Ortolani et al., xxx).

2. Experimental set up

The experimental activity was carried out at the outdoor maneuvering basin of the CNR–INSEAN located at the Nemi lake.

Ship selected for present analysis is the fast twin screw/twin rudder ship considered in (Coraddu et al., 2013; Ortolani et al., xxx). In table 1, principal geometric characteristics of the model and the propeller are reported in terms of ratio of ship length (L), beam (B), draft (T) and block coefficient (C_B).

The experimental layout is the same adopted in the (Ortolani et al., xxx); the model is equipped by IMU for the reconstruction of the motion, DGPS (differential GPS) and real time data transmission devices. Each propeller shaft is driven by a dedicated electric–brushless motor and is equipped by a dynamometer for the measurement of propeller thrust and torque. The starboard shaft was equipped also by a novel 2–component transducer [1] for the measurement of the bearing radial load. The whole energy demand of the on–board instruments was provided by a diesel electric generator.

In table 2 the test matrix of concern in present work is listed; in particular turning circles (with pull-out phase) and zig–zag maneuvers at different rudder angles were carried out. A tight zig–zag maneuver ($\pm 35°$) was also excecuted in order to realize a critical condition characterized by large amplitude motions during the transient as well and a relatively high (nominal) angle of attack in correspondence of the propellers (i.e., hull drift angle). All tests were carried out at constant propeller rate of revolution and in a real still weather environment, in order to avoid external disturbances.

Propeller forces and moments are made non–dimensional by the water density ρ, propeller revolutions N and propeller diameter D; unless otherwise specified, forces and moments are presented in terms of ratio with respect to values in the approach phase (identified with the subscript "0").

3. Data analysis

Due to the fact that the radial force components are measured with respect to a transducer that is fixed with respect to the maneuvering model, the measurements of K_{Ty} and K_{Tz} accounts both for inertial (accelerating mass) and hydrodynamic (caused by propeller hydro–loads) components, identified by the supercripts IN and HYD, respectively, as shown below:

$$
\begin{aligned}
F^b_{Ty} &= F^{HYD}_{Ty} + F^{IN}_{y} \\
F^b_{Tz} &= F^{HYD}_{Tz} + F^{IN}_{z}
\end{aligned}
\tag{1}
$$

[1] patent N. RM2014A000164

In order to get a closer insight on the phenomenology, the hydrodynamic contribution should be properly quantified; to this aim, for each component of the radial load, the inertial one can be determined, because the $6DoF$ motion of the model is measured and the masses involved (the propeller and the shaft) are known.

Introducing the weight of the propeller plus the shaft, M_p, and the vector of the linear accelerations $\dot{v^b}$ along the x, y and z axis of a representative point (r_P) on the shaft in the proximity of the radial force transducer, equation 1 can be expressed by:

$$
\begin{aligned}
F_{Ty}^{HYD} &= F_{Ty}^{b} - F_{y}^{IN} = F_{Ty}^{b} - M_p \dot{v^b} \\
F_{Ty}^{HYD} &= F_{Tz}^{b} - F_{z}^{IN} = F_{Ty}^{b} - M_p \dot{v^b}
\end{aligned}
\tag{2}
$$

The acceleration of r_P in the moving frame of reference can be determined by:

$$
\dot{v^b} = \dot{v} + \Omega \times v + \dot{\Omega} \times r_P + \Omega \times \Omega \times r_P \tag{3}
$$

where Ω, v (and their time derivatives) are the linear and angular velocities (accelerations) measured by the IMU (properly located close to the model's centre of mass).

It has to be remarked that the same approach was followed in (Ortolani et al., xxx): the measured loads were properly corrected for the centrifugal force only, because the analysis was focused on the steady phase of the turning maneuver and, therefore characterized by negligible accelerations.

The procedure to obtain the hydrodynamic contribution of the lateral and vertical components of the bearing radial force is schematized in figure 4; on the left and right figures the time histories of the loads during the initial transient of the turning circle at $F_N = 0.32$, $\delta = 35°$ are visualized, respectively. The procedure is summarized in the following points:

- the measured force (dotted black line) is corrected by removing the contribution of the propeller weight (Ortolani et al., xxx) (solid grey curve)
- the inertial contribution is then subtracted, to obtain the hydrodynamic load (solid red curve). In particular, it can be stressed that, in case of the horizontal component, the leading contribution of the apparent forces results from the centrifugal contribution $\Omega \times v$; on the other hand, the contribution of the inertial forces is negligible in case of the vertical force.

On this basis, it can be concluded that the origin of the peaks observed in the preliminary analysis in Part I are mainly related to the hydrodynamic performance of the propeller; in the following analysis this aspect will be thoroughly tackled; the superscript HYD is omitted to simplify the nomenclature.

4. Zig–Zag maneuvering performance

Before tackling the nature of the radial force in depth, the dynamic response of the model during the transients should be first discussed. The time histories of the zig–zag manoeuvers are shown in figure 3. In the upper figure the different phases of the zig–zag are identified by the rudder and heading angles, and the yaw rate. In both cases, between two consecutive yaw–reach points (rudder and heading angles are coincident), the model achieves a quasi–steady regime (the yaw rate is approximately constant). After the rudder is counter–actuated (at the yaw reach point), a snap–roll phenomena similar to that occurring during the start and the pull–out phase of the turning circle (Ortolani et al., xxx) is experienced by the model. However, in case of the zig–zag, the negative effect of the rudder is amplified, because it provides an opposite control force: as a result, the roll angle increases up to 40% with respect to the value of the quasi–steady phase. The variation of the pitch angle is negligible during the whole maneuver (less than $0.5°$) (see figure 3b). Despite at the highest rudder angle a roll–pitch coupling can be enforced, the roll speed is still prevalent with respect to pitch (see figure 3c), confirming that for these unsteady maneuvers the dynamic of the vessel can be synthesized by a $4DoF$ representation.

In table 3 the typical maneuvering characteristics of the zig–zag maneuvers are summarized in terms of overshoot angles and period (Lewis, 1998). Zig–zag tests were carried out until the 5^{th} overshoot phase was completed; the 2^{nd} overshoot angle is evaluated by averaging the values of the whole overshoot phase but the first one, because of their dynamic similarity and the geometrical symmetry of the model.

The maneuvering response at small rudder deflection is scarcely influenced by speed (the 1^{st} overshoot angle at F_N=0.26 and 0.32 are very similar); on the contrary, at the highest rudder angles (20°and 35°), both 1^{st} and 2^{nd} overshoot angles increase with speed (i.e., the yaw check ability of the model is worsened). The period of the maneuver obviously increases with the increase of the rudder angle and diminishes with the approach speed. The repeatability analysis is satisfactory, the $r.m.s$ being smaller than 10% as a whole and considering that the higher scattering of the data is observed for the 1^{st} overshoot angle at the lowest rudder angle.

5. Results – Phenomenological description

The physical aspects that rule the strong link between the bearing loads (on the internal and external shaft) and the motion of the model are synthesized considering different unsteady manoeuvres carried out at the approach speed $F_N = 0.32$. In particular, the bulk of the description is centred on the two transient phases successive to the the rudder actuation (i.e. start of the turn and pull-out phases, hereafter termed ST and PO, respectively); this choice is motivated by the fact that the transients are longer and are easier to identify (their are comprised between the approach and the turning) with respect to the other fully unsteady manoeuvres considered. Then, the developed concepts will be considered (and further strengthened) to synthesize the evolution of the in–plane loads in case of the zig–zag maneuvers ($\delta = \pm 20, \pm 35$) at the same F_N.

The reader has to be reminded that the propeller is termed "internal" when, during the maneuver, it is positioned in the leeward side with respect to the center of the turn, whereas it is specified "external" in the opposite case.

5.1. *Further consideration on the transient behavior of a propeller*

The correlation between the dynamic response of the model and the bearing loads is tackled by the aid of the simplified representation of the propeller operating at incidence described in (Ortolani et al. (xxx), section 3). It has to be stressed that this approach has to be considered an adequate characterization of the "mean" behavior of the propeller as long as the character of the inflow is quasi–steady (as it happens during the straight ahead condition or during steady phase of the turning maneuver). On the other hand, when the inflow conditions are time dependent, the propeller hydrodynamics is markedly affected by a phenomenon that is called "dynamic inflow" (Carpenter and Fridovich, 1953): in particular, the self–induction velocity field caused by the release of the vorticity from the propeller blades does not establish immediately as a consequence of the actual loading conditions. This can be physically interpreted by the fact that the state at regime will be achieved as long as the whole fluid of the propeller slipstream is accelerated to the value imparted by the new propeller loading condition. The lagging effect causes the blade sections to be impinged, immediately after the change of the inflow, by relative flow at an higher angle of attack (the self induction effect is still not developed) and, therefore, to develop higher loads. A more detailed and schematic description of the propeller operating in a fully unsteady regime is provided in (Amini and Steen, 2012) in the framework of $BEMT$ theory (Blade Element Momentum Theory). Following the same terminology provided in the above cited reference, the behavior of the propeller during transient conditions can be represented by an "inner" and an "outer" phenomenology: the former provides the local description of the propeller hydrodynamics (i.e., for the blade sections) whereas the latter provides the effective boundary conditions of the propeller itself (i.e. the effective angle of attack of the blade sections).

On this basis, the hydrodynamic contribution of the measured loads (equation 1) can be expressed as:

$$
\begin{aligned}
F_{Ty}^{HYD} &= F_y(v^b) + F_y(\dot{v^b}) \\
F_{Tz}^{HYD} &= F_z(w^b) + F_z(\dot{w^b})
\end{aligned}
\tag{4}
$$

where v^b and w^b, $\dot{v^b}$ and $\dot{w^b}$ represent the lateral and vertical components of the velocity and accelerations with respect to the bearing reference system. In order to evaluate and compare the contribution of the velocity and accelerations on the total force developed by the propeller, the acceleration dependent terms can be approximately evaluated in the framework of potential theory (Lamb, 1931; Carpenter and Fridovich, 1953), by the following expressions:

$$
\begin{aligned}
F_y(\dot{v^b}) &= 0.6637\frac{4}{3}\pi\rho v^b r^3 \\
F_z(\dot{w^b}) &= 0.6637\frac{4}{3}\pi\rho w^b r^3
\end{aligned}
\tag{5}
$$

where r represents the radius of the propeller. It has to be observed that the application of the above expression has to be considered an upper bound value, because in–plane acceleration rather than the lateral (and vertical) component of the total acceleration of the propeller are considered; however, for the purpose of the following description, aimed to qualitatively identify the sources and correlate them with motion, the above expression can emphasize the importance of considering this effect during typical transient maneuvers.

5.2. Transient Behavior of the Bearing radial force

The analysis is centered on the hydrodynamic component, obtained by removing from the measured forces the inertial contribution according to the methodology described in section 3. The effects of the motion on the generation of the in–plane loads is analyzed by postulating a strict relation between the velocities and accelerations caused by the motion and the radial force components on the basis of the simplified representation of the propeller operating at incidence (Ortolani et al., xxx) with the inclusion of the dynamic inflow effect. Within the transient phases, several instants (τ_1, τ_2, τ_3, and τ_4, τ_5 in case of the ST and the PO phase, respectively), representative of different attitude (i.e. propeller inflow) conditions of the model, have been selected.

5.2.1. External propeller

The radial force developed on the external propeller during the transient phases of a tight turning manoeuvre is discussed first; as it was observed in Part I (Ortolani et al., xxx), during the steady phase of the turning the inflow of the propeller located on the windward side resembles a pure oblique flow because the hull wake is deflected towards to the lee side. On this basis, the correlation between the forces and the motion should be better identified, it being scarcely affected by the additional perturbation of the hull wake.

In figure 5 the lateral and vertical components are visualized. The transient phase covers a limited interval of time (less than 10 seconds) after the rudder is actuated ($\tau_{\delta 0} = 10sec$) as highlighted by the time history of the roll angle. It has to be noticed that the rudder angle (dashed line) is reported as a fraction of its maximum value. In particular, in figure 6 the velocity and acceleration are distinctly represented for each motion (sway, roll and yaw) in the bearing frame of reference, in order to better highlight the correlation between the inflow (cause) and the force (effect) along the same direction.

After $t = \tau_\delta$, K_{Ty} monotonically increases and smoothly achieves a maximum value (close to $t = \tau_3$), few percent ($\sim 5\%$) higher than the value during the steady turn. The generation of the lateral force is mainly due to the sway and yaw velocities induced by the motion of the model, as clearly shown by the trend of the components of the lateral speed in figure 6a. The snap–roll ($\tau_\delta < t < 12sec$, negative roll angles) does not affect the evolution of the lateral force, its change of rate maintaining a constant value up to $t = \tau_2$. In fact, the roll induced velocity contributes for 8% (at $t = \tau_1$) and 3% (at $t = \tau_2$) of the resultant velocity v_{TOT}, providing a positive and negative contribution, respectively (see figures 7a and 8a on the left). The negative contribution of

$v(q)$ at $t = \tau_2$ is overcome by the increase of the sway and yaw induced velocities. Consistently, the lateral accelerations due to sway and yaw motions are dominant with respect to roll except in the the final instants of the transient, in the proximity of τ_3 (figure 6b). The hydrodynamic forces due to accelerations, i.e. the added mass, provide an additional contribution to the damping forces at $t = \tau_1$ and $t = \tau_2$ (see the left half of figures 7 and 8). However, the contribution of K_{Ty}^{ADM} seems not to provide a remarkable contribution during the whole transient, as it can be evidenced in figure 5 by comparison of the total hydrodynamic curve ($K_{Ty}H$) and the one that results from removing by it the added mass effect ($K_{Ty}DAMP$, solid blue line). In particular, as the lateral acceleration achieves its maximum (approximately at τ_2), the dynamic inflow effect contributes by less than 5% of $K_{Ty}H$.

The vertical component K_{Tz} (see figure 5b) exhibits an opposite trend with respect to K_{Ty}; after the rudder is actuated ($t = \tau_\delta$), it diminishes and establishes around a small, negative value during steady phase ($t > 25sec$). As discussed in Part I, this behavior has to be ascribed to the evolution of the hull wake during the motion. In fact, during the approach phase the propeller inflow (i.e. the hull wake) is upwardly directed, determining a vertical force that amounts to about 15% of K_{T0}; however, during the motion, the flow relative to the propeller is progressively oriented along the horizontal direction because of the sway–yaw induced motion and the consequent deflection of the hull wake to the lee side. The predominant (indirect) effect of the lateral velocity on the evolution of K_{Tz} is confirmed by the fact that the relative velocities and accelerations along the vertical axis z^b are almost an order of magnitude lower than the horizontal ones, as shown in figures 6c and 6d. Specifically, at $t = \tau_1$ the propeller experiences an up–ward motion that is caused by turning and roll, whereas the effect of v and the accelerations is negligible (see figures 6c–6d and the schematic outline on the right of figures 7a–7b). At $t = \tau_2$, during the restoring phase of the snap–roll, the inflow is oppositely directed and is responsible for a positive vertical force; both velocity and acceleration dependent terms are concurrent with the exception of $\dot{w}(p)$ (figures 7a–7b on the right). At about

$t = \tau_3$, K_{Tz} smoothly achieves a minimum and thereafter increases towards to the steady state value; in this case, the relative jump of the peak with respect to the stabilized one is greater than that observed in case of K_{Ty}.

It is worth of notice the completely different evolution experienced by K_{Ty} and K_{Tz} during the early phase of the transient ($\tau_\delta < t < \tau_2$): in particular, the slope m^Y_{1ST} of the lateral force is almost constant, whereas the vertical force shows a two steps rate of change. This behavior can be related to the character of the inflow during the approach phase: the monotone trend of K_{Ty} could be ascribed to the increase of the lateral flow induced by the motion. On the contrary, the initial reduction of K_{Tz} is caused by the progressive modification of the wake distribution over the propeller disk; the successive change of slope ($m^Z_{1ST} - m^Z_{2ST}$) could correspond to the progressive establishment of the pure oblique flow condition, i.e. the propeller disk cleaned from the hull wake (further deflected to the lee side). In both cases, the time histories in correspondence of the steady phase resemble the stabilization of the horizontal motion (sway and yaw induced velocities, see figure 6a).

The behavior of K_{Ty} and K_{Tz} during the pull-out phase is described in a similar fashion as above (see figures 9 and 10). After the rudder is removed back to zero ($t = \tau_\delta$) both the lateral and vertical forces smoothly restore around the value experienced during the straight ahead motion. During the early phase of the transient, the model shows a snap–roll behavior similar to that observed at the start of the maneuver and is essentially caused by the same counterbalancing effect provided by the hydrodynamic (due to hull and rudder) and inertial forces (centrifugal force applied to the model centre of mass) (Lewis, 1998; Ortolani et al., xxx). Moreover, the time histories of K_{Ty} and K_{Tz} evolve similarly towards to the straight ahead state, differently from what observed during the ST phase: in particular, their rate of change at first ($\tau_\delta < t < \tau_4$) is very slow (m^Y_{1PO} and m^Z_{1PO}), then increases ($\tau_4 < t < 99sec$, m^Y_{2PO} and m^Y_{2PO}) and once again drop during the stabilization. This behavior can be related to the lateral–roll response of the model. The relatively slow response of the model after the rudder actuation is due to the fact that the sudden increase of the roll angle improves the turning qualities of the model, causing it to be less reactive to external disturbances (i.e., the restoring hydrodynamic forces and moments) and, moreover, to the inertia of the model; this effect can be further highlighted by the slow variation of the propeller inflow along y^b and z^b (figure 10). After the snap–roll phase is completed ($t > 98sec$), the sway and yaw rate of the model were reduced by almost 80% and consequently, because of the small (restoring) hydrodynamic loads (the drift angle being small), the model smoothly achieves the rectilinear motion.

A closer inspection on the time histories of K_{Ty} and K_{Tz} is discussed below. At $t = \tau_4$, the combined sway–yaw and roll induced velocities and accelerations concur to reduce K_{Ty}. The sudden increase of the roll angle causes the propeller to shift along the positive direction of y^b; as a reaction, a negative damping force $F(v(p))$ arises. The damping forces, $F(v)$ and $F(v(r))$, diminish because of the reduction of v and $v(r)$; the inertial (added mass) effect, mainly determined by the sway and yaw rate (see figures 10a–10b and the left half of figure 11), concurs to reduce K_{Ty}, too. At $t = \tau_5$ the snap–roll phase is dying out; both lateral velocities and accelerations act to reduce the lateral force. It is interesting to notice that at the end of the snap–roll, the induced lateral speed in correspondence of the propeller is reduced by about 80% with respect to the value in the steady turning phase. The residual lateral force is still determined principally by v and $v(r)$ (the inertial effect due to both propeller weight and dynamic inflow effect is negligible).

The time history of K_{Tz} is shown in figure 9b. At $t = \tau_4$ the propeller inflow is not affected by the motion (see figures 10c and 10d). Thereafter, K_{Tz} suddenly increases: this behavior is not induced by the motion (the vertical component of the inflow diminishes) otherwise, it is a consequence of the progressive realignment of the hull wake and its re–distribution over the propeller disk; this is a plausible explanation, because, as it was stressed above, the lateral motion is reduced by about 80% at the end of the snap–roll phase (i.e., the angle of drift of the model is small). Subsequently ($t > \tau_5$) the vertical force increases slowly again (at a rate m^z_{3PO}), the straight motion being progressively achieved.

5.2.2. Internal propeller

The lateral and vertical components of the radial force generated on the internal shaft are now discussed in a similar style during the initial and pull–out transient of the turning manoeuver. Figures equivalent to 6, 7, 8, 10 and 11 are not repeated and can be easily adapted for the starboard manoeuver by properly inverting the sign of the terms considered. The phenomenological insight is carried out focusing on the same time instants already considered for the external shaft.

In figure 12 the time histories of K_{Ty} and K_{Tz} during the ST phase are shown. In general, it can be observed that both components exhibit a peaked trend that is completely different than that on the external shaft; the main reason for this discrepancy resides in the fact that, on the leeward side, the propeller hydrodynamics is profoundly affected by the hull wake. The assessment of the relation between the motion and the propeller in–plane loads, pursued by the previous analysis on the external shaft, allows to better identify and synthesize the key features of the propeller–wake interaction phenomenon. The variation of the horizontal component is represented in figure 12a; after the rudder is actuated ($t > \tau_\delta$), K_{Ty} decreases from positive to negative values. In fact, during the approach phase the transverse component of the inflow is positively directed (the flow "closes" at stern); during the turning ($STBD$ maneuver), the "average" flow relative to the propeller is directed to the leeward side, i.e. towards to the negative y^b direction (Ortolani et al., xxx). According to the dynamic response of the model represented in figures 6a and 6b, the reduction of K_{Ty} experienced during the snap–roll phase ($\tau_\delta < t < \tau_5$) is principally related to the damping forces induced by the sway–yaw motions (namely $F(v)$ and $F(v(r))$) that are predominant with respect to both the roll–induced one ($F(v(p))$) and the dynamic inflow effect. At $t = \tau_2$ the force exhibits a peak ($\Delta_{PEAK} = 23\%$ of K_{T0}) before increasing back to the steady value; the peak is particularly evident with respect that observed on the external propeller: in fact, focusing on the interval $\tau_2 < t < \tau_3$, it can be stressed that the variation of the force ($\Delta_{P-S} = 15\%$) is not consistent to the increase of the lateral velocity and acceleration, on the basis of the simplified representation of the propeller in oblique flow.

In figure 12b the time history of K_{tz} is depicted; in particular, during the snap–roll phase ($\tau_\delta < t < \tau_2$) K_{Tz} experiences an increase of about 70% and thereafter ($t > \tau_2$), it drops (approximately at the same rate) to the stabilized value lower than 70% than the peak. The velocities and accelerations (projected along the z^b axis) induced by the motion are completely uncorrelated to this behavior. The unique evolution of K_{Tz} highlights and further strengthens a phenomenology that is characterized by complex hydrodynamic interactions between the propeller and the hull wake. As a result, at $t = \tau_1$, the motion does not contribute to the vertical force (see figures 6c and 6d) and, at $t = \tau_2$ the roll damping force $F(w(p))$, oriented in the opposite direction with respect to the K_{Tz}, is generated (see figure 8a with the orientation of roll dependent terms inverted). Moreover, during the range of time $\tau_2 < t < \tau_3$, the lack of correlation between the dynamic response of the model and the vertical force (already observed for K_{Ty}) is confirmed, too. In particular, velocities (with the exception of $w(p)$) and accelerations are positive and, consequently, contribute to increase the value of K_{Tz} (with respect to $t = \tau_2$) that, otherwise, drops towards to the stabilized value. In other words, during the entire transient considered, the dynamics of K_{Tz} is completely affected by the evolution of the hull wake, i.e., its distribution over the propeller disc. As it will be emphasized in the following, the time varying evolution of the propeller inflow on the internal side is the key aspect at the basis of the peaked trend of the radial load components K_{Ty} and K_{Tz}.

The behavior of the internal propeller during PO is shown in figure 13. K_{Ty} smoothly converges towards to the steady value of the straight ahead sailing (figure 13a); the observed trend is mainly consistent to the drop of the lateral velocities caused by the combined reduction of the drift angle and yaw rate. It has to be remarked that the absence of a peak, does not exclude the occurrence of blade–hull wake interactions: in–fact, during the restoring straight ahead condition, the effects of the motion (reduction of the propeller developed load) on one side, and the hull wake distribution on the other, might compensate each other. After the actuation of the rudder ($t > \tau_\delta$), the slope of K_{Ty} is initially smaller than the rest of PO, because of the slow initial response of the model already described in 5.2.1.

The time history of K_{Tz} is represented in figure 13b; the behavior resembles that experienced after the start of the maneuver. Specifically, during the snap–roll phase ($t < \tau_5$), the load abruptly increase to a peak that is approximately 10% greater than the one occurred at $t = \tau_3$. As it was stressed above, this unique behavior is primarily determined by propeller–wake interaction phenomena, because the velocities and accelerations induced by the motion are barely correlated to the vertical force. In particular, for $\tau_\delta < t < 96.5sec$ the increasing trend of K_{Tz} is opposite with respect to the variation of the vertical components of velocities (see figure 10c); moreover, for $t > 96.5sec$ the drop of the vertical force seems to be excessively large to be related entirely to the vertical velocity and accelerations induced by the restoring motion.

5.2.3. Synthesis in terms of radial load and phase angle

The evolution of the bearing radial force and the phase angle contribute to synthesize the physical insight of results outlined above. To provide a schematic representation of the peculiarities at the basis of the phenomenology, the components of inflow field and the resultant one are cross–correlated for the representative time $t = \tau_2$ (occurrence of the peak) and are shown in figure 15.

The radial force and the phase angle (defined in equation (4) of Part I according to the reference system sketched in figure 2) on the internal (hereafter defined K_{Tr}^{INT} and ϕ^{INT}) and external (K_{Tr}^{EXT} and ϕ^{EXT}) propeller are depicted in figure 14 for ST and PO transients, respectively. During the ST (figure 14a), the radial force on the external shaft monotonically grows by about 90% (with respect to the value in the approach phase) and establishes around a slightly smaller value; K_{Tr}^{INT} follows a completely different trend that resembles that of

K_{Tz}^{INT}; in particular, it quickly increases and, after achieving a peak (lower than that on the external side) drops to the steady value. It is worth of noticing that the higher grow rate of K_{ST}^{INT} with respect to K_{ST}^{EXT} (slopes m_{1ST}^{RI} and m_{1ST}^{RE}) is a symptom of the dynamics of the wake past the hull and its interaction with the propeller.

The trend of the phase angle highlights that the inflow on the internal propeller is not totally induced by the motion of the model. In fact, after the start of the maneuver, ϕ^{EXT} increases and achieve a value around 90°, i.e., K_{Tr}^{EXT} is oriented horizontally, consistently to the fact that the propeller experiences a pure oblique flow (figure 15). On the contrary, on the leeward side, the phase angle stabilizes around $\phi = -50°$, the inflow being characterized by a relevant vertical component, too. This effect is not directly correlated with the dynamic response and the lack can only be solved if the contribution of the hull wake is taken into account (figure 15). Furthermore, the evolution of ϕ^{INT} shows a change of slope in correspondence of the peak, probably because of the drop of K_{Tz}^{INT} (m_{1ST}^{ϕ} and m_{2ST}^{ϕ}).

During the pull–out phase, the behavior of the radial load is strongly affected by the vertical component on the internal side, as it can be evidenced by the strong peak achieved in the during the snap–roll (figure 14b). However, after the rudder actuation, the increase of K_{Tr}^{INT} is smaller than the jump of K_{Tz} (figure 13b) and conversely, the drop towards to the stabilized value is higher. Across the peak the rate of change of K_{Trad} is discontinuous, as it was observed during ST. On the windward side, the behavior of K_{Tr}^{EXT} resembles the smoother trend outlined by both K_{Ty} and K_{Tz} (figure 9).

5.3. Transient Behavior of the Bearing radial force during zig–zag maneuvers

The phenomenology outlined for the transient phases of the turning circles is further inspected by analyzing the zig–zag maneuvers. In figures 16 and 17 the time histories of the radial force, phase angle and the vertical and horizontal components are depicted for the ±35° and ±20° maneuvers, respectively. Because of the oscillatory character of this kind of tests, the propeller periodically operates on the wind and the lee side; in figures 16 and 17 three consecutive phases are identified: during I_1 and I_3 the propeller is internal, whereas during E_2 the propeller is external. Consistently to the description of the turning circle, ST^i and a PO^i transients (i referring to the specific phase) can be identified to the time intervals the rudder is going to be established and immediately after the counter actuation of the rudder at the yaw reach point, respectively. In the following, the correlation between the loads and the dynamic response of the model is omitted because the main concern of the following discussion is to provide a support to the idea developed in section 5.2.

In order to ease the comparison with the transient phases experienced during the 35°turning circle, it is better to start the analysis with the ±35° zig–zag.

Generally, during each phase the evolution of K_{Ty} and K_{Tz} (figure 16a) resembles the same features observed during the ST and PO phases of the turning circle, experienced both by the internal and external propeller. In fact, during the ST phase of I_1 and I_3 (the propeller is internal), K_{Ty} drops to a negative value whereas K_{Tz} increases and after the yaw reach point ($t = 16$ and $t = 53$, respectively) suddenly recover the value of the approach phase. Both loads evidence a peaked character during $ST^{1,3}$ and $PO^{1,3}$; the magnitude of the peaks is very similar to those experienced during the transients of turning circle. The peaks of the vertical component (Pk_1^Z, Pk_2^Z, Pk_3^Z, Pk_4^Z) are remarkably stronger with respect to the horizontal ones (Pk_1^Y, Pk_3^Y); the peaks of K_{Tz} experienced during $PO^{1,3}$ are slightly higher with respect those at $ST^{1,2}$. When the propeller is external (phase E_2), during ST^2, K_{Ty} increases and, after experiencing a maximum (Pk_3^Y), stabilizes around a smaller value; on the contrary, K_{Tz} drops to negligible (negative) value, consistently to the fact that the inflow to the propeller is directed almost horizontally and is not affected by any disturbance from the hull. It has to be pointed out that the onset of the peak Pk_2^Y (not observed during the turning circle) is a consequence of the larger motion of the model owing to the higher excursion of the heading angle after the first yaw reach point ($t = 16.5sec$). Finally, during PO^2 both components smoothly recover those of the approach phase.

The time histories of the radial force and the phase angle is depicted in figure 16b. The evolution of K_{Tr} is strongly affected by K_{Tz} when the propeller is internal, as it can be evidenced by the close similarity of their shape during I_1 and I_3; during E_2 the radial force is entirely determined by the lateral force, K_{Tz} being very small. The radial force increases up to 70% and up to above 100% (with respect to K_{Tr0}) on the internal and external propellers, respectively. Finally, the variation of the phase angle is consistent to the fact that the radial force is directed almost horizontally on the external shaft ($\phi^{EXT} \sim 90°$, during E_2) and at about $\phi^{INT} = -55°$ when the propeller is internal (phase I_1 and I_3).

The comparison with the $\pm 20°$ maneuver allows to draw further considerations about the development and evolution of the bearing radial force, with particular emphasis on the internal shaft. It can be clearly observed from figures 17a and 17b that the behavior of K_{Ty} and K_{Tz} (and therefore, K_{Trad} and the phase angle) during E_2 (the propeller is on the wind side) is qualitatively similar to the correspondent phase of the $\pm 35°$ maneuver. In fact, during the interval ST^2 ($18.5sec < t < 25sec$), the horizontal force increases whereas the vertical one diminishes owing to the establishment of a pure oblique flow condition to the propeller; then a radial force directed almost horizontally ($\phi \sim 85°$) results. The strict link with the horizontal motion is emphasized by the smaller magnitude of K_{Ty}, consistent to the lower amplitude of the effective drift angle to the propeller induced by the sway and yaw motions. The absence of a correspondent peak in case K_{Ty} can be explained by the more moderate amplitude of the motions.

On the contrary, the time history on the internal shaft (phases I_1 and I_3) highlights some interesting features by comparison with the tighter zig–zag (see figure 16a). In particular, peaks are still evident at the begin (ST^1 and ST^2) and the end (PO^1 and PO^3) of each phase only in case of K_{Tz}; although their magnitude is very similar to the tighter maneuver ($\Delta_{PEAK} \sim 35\%$), the subsequent drop in the central part ($14sec < t < 17.5sec$ and $38sec < t < 44sec$) is small. Otherwise, the evolution of K_{Ty} is smooth and its magnitude (lower with respect to the $\pm 35^\circ$ maneuver) seems to be more sensitive to the amplitude of the lateral motion. As a result, the time history of K_{Trad} is free from the strong peaks characteristics of the maneuver at the highest rudder angle, although the maximum values are almost equal.

The non–linear character evidenced in case of K_{Tz} during the two transient maneuvers at different rudder angle further emphasizes the fact that performance of the internal propeller markedly depends on propeller wake interaction. This behavior is obviously affected by the character of the motion, it affecting the wake evolution past the hull and, consequently, its distribution over the propeller disk. An alternative perspective on the nature of the phenomenology can be further stressed observing the evolution of the phase angle: on the external shaft it is almost constant, remarking the fact that the character of the inflow to the propeller maintains similar with the variation of the magnitude of the motions; on the contrary, on the internal shaft, it experiences larger changes caused by non–similarity of the effect induced by the motion on the internal propeller, which may be explained with the marked non–linear evolution of the hull wake.

6. Results – Data analysis

The experimental data are systematically analyzed in terms of rudder angles at the three different approach speeds. The phenomenological insight described in the previous section provides physical–based background to interpret the experimental data; on the other hand, the systematic overview of the data allows to completely identify and generalize the key aspects of the physic affecting the generation of the in–plane loads.

The systematic analysis is focused on the hydrodynamic contributions of the propeller in–plane loads (i.e. the effect of propeller weight and inertial contributions are removed from the measured values). The results of the peaks of the radial force and the in–plane components are presented in terms of mean value and standard deviation (*r.m.s.*); the average value is expressed in terms of ratio with respect to the propeller thrust during the approach phase (K_{T0}), whereas the $r.m.s$ (evaluated on the dimensional value) is reported in terms of a percentage of the averaged one. The reliability of the experimental tests was assessed by repeating at least 4 times all the tests. Turning circles at ±35° and zig–zag ±20°, ±35° were repeated 8 times, because these condition are the most critical one in terms of the dynamic response of the vessel and the operating conditions of the propellers.

In order to better detect some interesting features on the nature of the transient loads, the peaks have been further inspected in terms of percentage variance with respect to the value experienced during the approach (in case of the stabilized values) and the steady phase (transient peaks), according to the following expression:

$$\begin{aligned} \Delta K^{P-0}_{T_{rad,y,z}} &= \frac{K^{PEAK}_{T_{rad,y,z}} - K^{0}_{T_{rad,y,z}}}{K_{Tr0}} * 100 \\ \Delta K^{P-S}_{T_{rad,y,z}} &= \frac{K^{PEAK}_{T_{rad,y,z}} - K^{STAB}_{T_{rad,y,z}}}{K_{TrSTAB}} * 100 \end{aligned} \tag{6}$$

It has to be observed that the choice of K_{Tr} (in the denominator) allows to prevent ratio with small quantities in case of the horizontal (during the approach phase) and the vertical components (during the steady phase, external propeller).

The time histories of both the dynamic response (figure 3) and the propeller (in–plane) loads (figure 16 and 17) highlight the low frequency nature of the zig–zag maneuver. In fact, the yaw–rate achieves a quasi–state regime prior to the yaw reach (see figure 3a) after the 1^{st} overshoot. Moreover, the transient propeller loads are remarkably similar to that experienced during the ST and PO phases of the turning circle, in particular the vertical component K_{Tz}. On this basis, data of both maneuvers were jointly visualized in order to increase the sampling in the range of rudder angles considered as well as to provide a broader overview of the phenomenon in figures 18–20. The peaks of K_{Ty}, K_{Tz}

(ratio with respect to the K_{T0}) and the radial force (both in terms of ratio with respect to K_{T0} and K_{Trad0}, hereafter termed K^{T0}_{Trad} and K^{R}_{Trad}, respectively) experienced during the transient phases (ST and PO) of the turning circle and zig–zag are considered; in particular, on the left columns the peaks are shown in terms of ratio with respect to K_{T0}. The stabilized values are also included in order to emphasize the differences between the steady and the transient phases. On the right columns, moreover, peaks evaluated according to equation 6 are visualized; in case of the zig–zag, only the 35°maneuver is considered due to the lack of stabilized values at 10°and 20°.

For the sake of clarity, however, the results of the turning circles are first discussed, and then discrepancies and similarities with respect to the zig–zag data will be pointed out.

The maximum transient values of vertical and horizontal components of the in–plane loads are listed for the ST and PO phases and are visualized in figures 18 and 19 in tables 5 and 6.

The repeatability of the loads is satisfactory both on the internal and external propeller; increasing the approach speed, the scatter is reduced, this being apparently a consequence of the relative increase of the mean value of the propeller loads with respect to the maximum variation. This observation also motivates the discrepancies of the scatter between the vertical and horizontal components of the loads on the internal and external shaft, respectively. In fact, on the internal shaft, the *r.m.s.* of K_{Tz} is 10% lower than the mean values at $F_N = 0.26$ and it is further reduced below 6% at the highest speeds; furthermore, the scatter of K_{Ty} is larger with respect to the vertical components, in particular, at the lowest F_N, σ greater than 20% results, at $\delta = 15°$ (both at ST and PO) and $\delta = 35°$. On the external shaft, the previous trend is completely reversed: the *r.m.s.* of K_{Tz} is 30% higher than the averaged values at the lowest speed and slightly improves (up to 20%) at $F_N = 0.32, 0.36$, whereas the scatter of the horizontal component is reduced to below 10%. This different trend can be explained by the fact that, on the leeward side, the magnitude of K_{Tz} is greater than K_{Ty} at the various regimes whereas, on the windward side, this trend is reversed, as it can be easily checked by inspection of tables 5 and 6. According to the phenomenological description in section 5.2.1, the lateral component does not experience peaks during the pull–out phase and therefore, only the ST phase is reported.

On the left of figure 18 the global behavior of the horizontal component is depicted in terms of the stabilized (black squares) and peaks values (experienced at ST and PO, represented by blue colored triangle and a green colored square, respectively); the magnitude experienced during the approach phase is reported by a dashed, red line.

In general, on the internal side (i.e. $\delta > 0$) the peaks of K_{Ty} during the ST show a similar trend with respect to the stabilized phase (lowest and medium speeds) at $\delta = 15°$ and $25°$ whereas, at the highest rudder angle, their rate of change can be glimpsed. During the pull–out phase, the peaks are considerably smaller with respect to those occurring at the start of the maneuver, their value being approximately close to the stabilized one (see also the time history of K_{Ty} represented in figure 12a). The percentage increase of peaks with respect to the stabilized value (evaluated according to equation 6), shown on the right of figure 18, is almost linear with rudder angles. The slope of Δ^{P-S} diminishes with the increase of speed in the low to medium F_N range (the peaks at $\delta = 35°$ amount to 50% and 35% of K_{Ty}^{STAB} at F_N=0.26 and 0.32, respectively), whereas it seems to be almost constant at the higher speed.

The trend of the peaks experienced by the external propeller ($\delta < 0$) with rudder angle follows approximately the stabilized values, as previously observed for the internal propeller. The peaks of K_{Ty} are considerably higher (almost doubled) with respect to those on the internal shaft, consistently to the fact that the propeller inflow is characterized by a predominant lateral component owing to the negligible perturbation induced by the upstream presence of the hull. However, it can be emphasized that the difference with respect to the stabilized values is smaller with respect that observed on the leeward side (pictures on the right of figure 18). This different behavior is determined by the smooth variation of the lateral component of the inflow, it being strictly related to the lateral motion of the model. On the contrary, on the leeward side, the discrepancies between the transient and stabilized values are caused by the evolution of the wake past the hull during the transients, affecting the magnitude and distribution of the inflow to the propeller. According to the phenomenological description in section 5.2.1, the lateral component does not experience any relevant peak during the pull–out phase and therefore, only those occurring during the ST phase are depicted.

The general behavior of K_{Tz} is shown on the left of figure 19. On the leeward side, the trend of the peaks is scarcely correlated to the variation of the stabilized value K_{Tz}^{STAB}; in particular, the magnitude of the peaks is almost constant with rudder angles, with the sole exception of the turning circle maneuver at $\delta = 35°$, $F_N = 0.26$. Contrarily to the horizontal component, the peaks experienced during the pull out phase are almost equal, or even greater than those occurring at the start of the maneuver (i.e. $\delta = 25°$ and $\delta = 35°$, respectively at $F_N = 0.26$ and $F_N = 0.32, 0.36$). Also in this case the variation of the peaks with rudder angle seems to be scarcely affected with change of the rudder angle; from a different perspective, it can be hypothesized that the peaks experienced of the internal propeller are caused by specific propeller–wake interaction that arise at drift angles that are smaller, or at least equal, to that experienced by the model during the steady turning phase at $\delta = 15°$ (i.e., small drift angles).

The trend of the percentage increase of the peaks with respect to the stabilized value (equation 6) shows an almost non–linear character with rudder angles and speeds. In particular, the rate of change of $\Delta_{K_{Tz}}^{P-S}$ at F_N=0.26 decreases at highest rudder angles, whereas it is monotonically increasing at the intermediate speed; moreover, $\Delta_{K_{Tz}}^{P-S}$ is progressively reduced as long as the the speed increases. The considerably higher values of Δ^{P--S} emphasize that the transient behavior of K_{Tz} is globally stronger with respect to the K_{Ty}. On the windward side, the absolute values of the peaks is considerably smaller with respect to the leeward side, being the propeller inflow (and therefore, the propeller developed radial force) horizontally directed. Analogously to the general behavior observed for K_{Ty}, the discrepancies of the peaks with respect to the stabilized value is lower than that observed on the internal side owing to the completely different features of the inflow (i.e., the data are less scattered).

For the sake of completeness, the peaks of the radial loads and the $r.m.s.$ are summarized in tables 7 and 8 for the internal and the external propeller, respectively. In particular, the radial force is evaluated in terms of a ratio with respect to the thrust and the radial force experienced during the approach phase (second and third column in the tables, respectively). The repeatability of the peaks is satisfactory and improves with the nominal speed of the tests. On the windward side, peaks occurring during the PO phase are not included in the table, consistently to the fact the radial force shows a similar trend of K_{Ty} (see discussion in section 5.2.3). The variation of K_{Trad}^{T0} is visualized in figure 20. In general, the character of the radial force synthesizes the features observed for K_{Ty} and K_{Tz}. On the external side the trend resembles that of the horizontal component whereas, on the lee side the trend is driven by the vertical force. The scatter of the peaks with respect to the stabilized values is considerably smaller in case of the external propeller than the internal one; this is evidenced by the higher value of Δ_{KTrad}^{P-S} on the internal propeller (pictures on the right side of figure 20). Finally, it is worth of noticing that during the transient phases the radial force achieves values 200% and 240% higher than the radial force experienced during the approach phase on the internal and external shaft, respectively (see also tables 7 and 8).

The peaks of the K_{Ty}, K_{Tz} as well as their $r.m.s$ experienced during the zig–zag maneuvers are summarized in tables 9–10. In the tables, two different values of the peaks are reported, namely the averaged value occurring up to the conclusion of the first overshoot phase (inside the brackets) and the averaged ones evaluated during the entire maneuver. Also in this case the repeatability analysis can be considered satisfactory, the character of σ at the different rudder angles and speeds being consistent with that observed for the ST and PO phases of the turning maneuvers.

The peaks experienced during the zig–zag maneuvers are visualized in figures 18–19 (distinguished by the empty symbols). Globally, the zig–zag data fit the trend of the turning circle; this fact has to be ascribed to the intrinsically low frequency features of the zig–zag maneuvers and, moreover, to the marked correlation of the occurrence of the peaks with the kinematic response of the model, as already discussed in section 5.3. Moreover, it is interesting to notice that the difference between the peaks evaluated considering the first overshoot phase (subscript $1ov$) and the whole maneuver (subscript $unst$) are not negligible, in particular at the highest rudder angle ($\delta = 35°$). In particular, the peak occurring during the first transient is stronger with respect to the successive ones. This is due to the fact that, with the increase of the rudder angle, the dynamic response of the model during the first overshoot is faster (as proved by the overshoot angles in table 3); as a consequence, the in–plane velocity components could result higher with respect to those of the successive cycles.

For the sake of completeness, peaks of K_{Trad}^{T0} and K_{Trad}^{R} (as well as the $r.m.s.$ of the radial force) are summarized in tables 11 and 12; the former representation is depicted in figure 20. Aspects concerning the repeatability as well as the trend with rudder angles and speeds are qualitatively similar to those discussed for the vertical and horizontal components and are not repeated.

6.1. Synthesis

The systematic analysis of the transient loads highlights a very interesting aspect that is complementary to the analysis outlined in sections 5 and allows to gain a deeper understanding of the phenomenology that affect the generation of the transient radial loads on the internal propeller. On the leeward side, in fact, the propeller performance is profoundly determined by complex hydrodynamic interactions with the hull wake with respect to the windward side where the propeller performance is mainly characterized by the dynamic response of the model. The systematic investigation highlighted, on the internal shaft, that the trend of the peaks (in particular those related to the vertical force K_{Tz}) is almost constant with the increase of the rudder angles whereas this correlation is remarkable in case of the stabilized values. In other words, the occurrence of the peaks is caused by a phenomenon, presumably related to the evolution of the wake past hull, that is experienced at drift angle that should be smaller than the one experienced at lowest rudder angle; to better represent this peculiar aspect, in figure 21 the time hystories of the TR and PO phases of the turning circle at three different rudder angle at $F_N = 0.32$ are reported. Three peculiar aspects has to be higlighted:

- after the rudder is actuated (t=τ_δ) the vertical force experiences a marked and similar increase (Δ_{P-S}) during all maneuvres;
- after the peak, the loads converge towards to a stabilized value that is inversely proportional to the rudder angle;
- during the pull–out of the tighter maneuvers ($\delta = 25°, 35°$), as long as the model is going to recover the straight ahead path, the propeller experiences a further peak, characterized by a similar magnitude as the former one; on the contrary, in case of the turning at $\delta = 15°$, the vertical force diminishes to the straight ahead value.

The particular trend of the vertical force observed above can be explained considering that:

- the hull wake evolves during the motion, namely it is always convected with the local velocity field; i.e., during the ST phase it progressively deflects and after the rudder removal it realigns to the symmetry plane of the model.
- the morphology of the wake, and therefore the propeller inflow, changes (in terms of both magnitude and distribution of the velocity components over the propeller disk)
- the in–plane loads are profoundly affected by the distribution of the wake over the propeller disk; in other words, the more a perturbation of the propeller infow is asymmtrically distributed over the disk, the higher the developed in–plane force will result.

During the maneuver, therefore, the hull wake is deflected towards to the internal propeller as schematically represented in figure 22a: the higher the rudder angle, the more the wake would be deflected laterally with respect to the propeller with a particular distribution over the propeller disk. To explain the occurrence of the peaks, the existence of a critical wake deflection that is approximately coincident to the wake deflection experienced at $\delta = 15°$ can be postulated; as schematically represented, the wake along the critical path would promote an asymmetric distribution of the inflow over the propeller, its interaction with the propeller being limited to a small portion of the disk only. As a result, the in–plane loads would rise considerably. Increasing the rudder angle, the wake is further deflected towards to the propeller; the perturbation to the inflow would be more homogeneously distributed over the disk and, consequently the generation of the side force should be smaller. For the sake of clarity, these concepts are useful to provide a "dynamic" description of the transient phases ST of the turning circle maneuvres at $\delta = 15°$ and $\delta = 35°$, schematically represented in figures 22b and 22c. In the former case, after the rudder excecution, the perturbation of the wake shifts towards to the propeller disk in $zoneA$. At a representative position, this perturbation at $t = t_T$ upset the distribution of the propeller inflow owing to its evolution during the motion; in particular, the hydrodynamic of the blades during the dowstroke phase of the rotation (blade positions 123) would be affected. As a consequence, the radial force (and its components) increases, determining the peak Δ_{P-S} in figure 21. Thereafter, the model gradually achieves the steady phase of the turn, that, in case of the lowest rudder angle causes the wake to be still positioned in the proximity of the critical region; as a consequence, the loads during the stabilized phase should be very similar to the previous increase experienced at $t = t_T$. On the contrary, in case of the tighter maneuver, the steady turn attitude of the model induces a larger deflection of the wake and probably a more regular distribution over the propeller disk that causes the abrupt reduction of the in–plane force ($t = t_S$ in $zoneB$, see figure 22c). This heuristic representation also support the behavior during the pull-out phase (omitted for the sake of brevity).

This interpetation does not pretend to represent exhaustively the extremely complicated hydrodynamic phenomena that affect the propeller–wake interaction; instead, it is aimed to provide a phenomenological synthesis entirely developed by the thorough inspection and analysis of the experimental data.

7. Conclusion

Present work aims to investigate the nature of the bearing radial loads generated by a marine propeller during the transient phases of a maneuver, further extending the work described in Part I, principally devoted to their quantification during quasi–steady operational conditions (straight ahead and steady turning). The measurements of the in–plane loads allowed to improve the actual state of the art methodologies of free running model test set–up and their potential capability to investigate very complicated hydrodynamic phenomena related to propeller hydrodynamics operating in design and off–design conditions whose identification, otherwise, would not be as much immediate by the sole measurements of thrust and torque. The analysis was carried out both in a phenomenological style on reference maneuvers and systematically analyzing the data in terms of rudder angles and speeds. The synthesis of both perspectives was reliable to interpret the experimental data and identify the key features governing the generation of the propeller radial force. In particular, in case of a twin screw ships, the transients phases are critical for the internal shaft, because of very complicated propeller–wake interactions; these results in strong peaks that occur immediately after the rudder actuation, and therefore, at small drift angles. In fact, in this circumstance, the deflection of the upstream hull wake would modify the propeller inflow over a limited area of the disk, inducing a asymmetric distribution that may markedly affect the development of stronger in–plane forces. Present conclusion are not definitive and further research is necessary to gain a deeper insight into these aspects; in particular, the evolution of the wake and the way it modifies the propeller inflow distribution at relatively small angles of drift (both after the rudder actuation and during pull–out like phases) would certainly clarify some key features of the interaction with the propeller.

ACKNOWLEDGMENTS

This research activity is funded by the Flagship Project RITMARE - The Italian Research for the Sea – coordinated by the Italian National Research Council and funded by the Italian Ministry of Education, University and Research within the National Research Program 2011-2013. The authors would like to acknowledge the technical group involved to the design and manufacturing phases of the transducer: Ing. M.Masia, R.Zagaglia, M. Sellini and A.Sabelli. The authors are also grateful to S.Principe, V.Giorgi, M.Orrico and L.Gatti for their support during the execution of the free running model tests.

References

Amini, H., Steen, S., 2012. Theoretical and experimental investigation of propeller shaft loads in transient condition. International Shipbuilding Progress 59, 55–82. doi:10.3233/ISP-2012-0079.

Atsavapranee, P., Miller, R., Day, C., Klamo, J., Fry, D., 2010. Steady-Turning Experiments and RANS simulations on a Surface Combatant Hull form (Model#5617), in: Proc. of 28th Symposium on Naval Hydrodynamics, Pasadena, California.

Carpenter, P., Fridovich, B., 1953. Effect of a rapid blade–pitch increase on the thrust and induced velocity response of a full scale helicopter rotor. Technical Report No. TN 3044. National Advisory Committee for Aeronautics (NACA).

Coraddu, A., Dubbioso, G., Mauro, S., Viviani, M., 2013. Analysis of twin screw ships' asymmetric propeller behaviour by means of free running model tests. Ocean Engineering 68, 47–64. doi:10.1016/j.oceaneng.2013.04.013.

Gurr, C., Rulfs, H., 2008. Influence of transient operating conditions on propeller shaft bearings. Journal of Marine Engineering and Technology A012, 3–11.

Lamb, J., 1931. Hydrodynamics. first ed., Dover, New York.

Lewis, J., 1998. Principles of Naval Architecture - vol. 3. second ed., SNAME, New York.

Ortolani, F., Mauro, S., Dubbioso, G., xxx. Influence of transient operating conditions on propeller shaft bearings. submitted to Ocean Engineering xxx, xxx.

Vartdal, B., Gjestland, T., Arvidsen, T., 2009. Lateral Propeller Forces and their effects on Propeller Shafts Bearings, in: Proc. of 1^{st} Symposium on Marine Propellers and Propulsion, Throndheim, Norway.

MODEL DATA	
L/B	7.5
B/T	3.25
C_B	0.5
Number of blades (Z)	5
Pitch ratio (P/D)	1.35
Expanded area ratio	0.79
Hub ratio	0.250

Table 1: Geometric characteristics of the ship and propeller model

FREE RUNNING TESTS		
TEST	SPEED	rudder angle [deg]
turning circle (with pull–out)	$F_N = 0.26, 0.32$	$\delta = \pm 15°, \pm 25°, \pm 35°$
turning circle (with pull–out)	$F_N = 0.35$	$\delta = \pm 35°$
zig–zag	$F_N = 0.26, 0.32$	$\delta = 10° - 10°, 20° - 20°, 35° - 35°$
zig–zag	$F_N = 0.35$	$\delta = 10° - 10°, 20° - 20°, 35° - 35°$

Table 2: Test matrix

$F_N = 0.26$					
δ	1^{st} ov. [deg]	σ %	2^{nd} ov. [deg]	σ %	period
10°	5.57	16.8	6.01	9.92	278
20°	14.41	7.1	14.69	5.6	324
35°	27.24	10.5	24.79	7.69	434
$F_N = 0.32$					
δ	1^{st} ov. [deg]	σ %	2^{nd} ov. [deg]	σ %	period [sec]
10°	7.09	6.8	7.64	4.5	229
20°	18.48	7.3	18,24	3.9	273
35°	34.4	5.98	31.67	6.8	361
$F_N = 0.35$					
δ	1^{st} ov. [deg]	σ %	2^{nd} ov. [deg]	σ %	period
20°	17.79	1.0	18.53	4.7	257
35°	37.12	4.5	36.48	3.6	343

Table 3: Results of zig–zag tests. Typical parameters

time	$\frac{v}{v_{TOT}}$	$\frac{v(p)}{v_{TOT}}$	$\frac{v(r)}{v_{TOT}}$	$\frac{w}{w_{TOT}}$	$\frac{w(p)}{w_{TOT}}$	$\frac{w(r)}{w_{TOT}}$
τ_1	0.06	0.129	0.805	-($w_{tot} \sim 0$)	-($w_{tot} \sim 0$)	-($w_{tot} \sim 0$)
τ_2	0.456	-0.0186	0.571	-0.33	0.87	0.46
τ_3	0.527	-0.002	0.474	0.572	-0.06	0.49
τ_4	0.575	-0.0075	0.43	0.642	-0.095	0.45
τ_5	0.648	0.0445	0.305	0.395	0.351	0.251

Table 4: velocity components due to the motion

$F_N = 0.26$				
δ [deg]	$\sigma_{K_{Ty}}$ %	$\sigma_{K_{Tz}}$ %	K_{Ty}	K_{Tz}
15° (TR)	22	4.7	-0.176	0.31
25° (TR)	3.2	5.6	-0.21	0.308
35° (TR)	9.4	4.2	-0.192	0.239
15° (PO)	27	7.4	-0.124	0.286
25° (PO)	4.35	8.84	-0.18	0.327
35° (PO)	21.7	8.38	-0.121	0.239
$F_N = 0.32$				
δ [deg]	$\sigma_{K_{Ty}}$ %	$\sigma_{K_{Tz}}$ %	K_{Ty}	K_{Tz}
15° (TR)	3.38	2.8	-0.143	0.256
25° (TR)	1.9	0.07	-0.17	0.26
35° (TR)	6.68	5.45	-0.186	0.242
15° (PO)	10.9	3.02	-0.109	0.257
25° (PO)	2.95	1.31	-0.143	0.258
35° (PO)	11.7	3.6	-0.143	0.254
$F_N = 0.35$				
δ [deg]	$\sigma_{K_{Ty}}$ %	$\sigma_{K_{Tz}}$ %	K_{Ty}	K_{Tz}
35° (TR)	4.62	5.77	-0.186	0.216
35° (PO)	8.89	4.68	-0.143	0.234

Table 5: Bearing forces on the internal shaft. Turning Circle

$F_N = 0.26$				
δ [deg]	$\sigma_{K_{Ty}}$ %	$\sigma_{K_{Tz}}$ %	K_{Ty}	K_{Tz}
15° (TR)	2.9	14.5	0.240	-0.028
25° (TR)	2.8	30.45	0.367	-0.0954
35° (TR)	4.0	20.5	0.363	-0.078
15° (PO)	4.2	18.0	0.24	-0.016
25° (PO)	7.45	38.8	0.349	-0.034
35° (PO)	9.8	35.8	0.335	-0.03
$F_N = 0.32$				
δ [deg]	$\sigma_{K_{Ty}}$ %	$\sigma_{K_{Tz}}$ %	K_{Ty}	K_{Tz}
15° (TR)	5.0	25.5	0.272	0.004
25° (TR)	5.02	20.6	0.338	-0.044
35° (TR)	5.09	33.5	0.33	-0.05
15° (PO)	3.5	17.6	0.240	0.064
25° (PO)	2.6	14.3	0.33	-0.030
35° (PO)	5.17	38.9	0.327	-0.024
$F_N = 0.35$				
δ [deg]	$\sigma_{K_{Ty}}$ %	$\sigma_{K_{Tz}}$ %	K_{Ty}	K_{Tz}
35° (TR)	6.5	20.2	0.322	-0.045
35° (PO)	4.1	21.4	0.320	-0.037

Table 6: Bearing forces on the external shaft. Turning circle

$F_N = 0.26$			
δ [deg]	$\sigma_{K_{Trad}}$ %	K_{Trad}^{T0}	K_{Trad}^{R}
15° (TR)	4.48	0.332	2.135
25° (TR)	3.32	0.341	2.191
35° (TR)	4.3	0.253	1.652
15° (PO)	1.9	0.299	1.925
25° (PO)	16.8	0.345	2.191
35° (PO)	9.99	0.245	1.600
$F_N = 0.32$			
δ [deg]	$\sigma_{K_{Trad}}$ %	K_{Trad}^{T0} %	K_{Trad}^{R}
15° (TR)	1.73	0.283	1.767
25° (TR)	0.63	0.303	1.943
35° (TR)	5.4	0.273	1.734
15° (PO)	2.53	0.271	1.693
25° (PO)	0.31	0.272	1.747
35° (PO)	4.72	0.266	1.687
$F_N = 0.35$			
δ [deg]	$\sigma_{K_{Trad}}$ %	K_{Trad}^{T0} %	K_{Trad}^{R}
35° (TR)	4.1	0.262	0.262
35° (PO)	4.6	0.245	0.245

Table 7: Modulus of the radial force on the internal shaft. Turning circle

$F_N = 0.26$			
δ [deg]	$\sigma_{K_{Trad}}$ %	K_{Trad}^{T0} %	K_{Trad}^{R}
15° (TR)	2.80	0.25	1.71
25° (TR)	0.95	0.378	2.41
35° (TR)	3.9	0.365	2.50
15° (PO)	5.5	0.240	1.72
25° (PO)	7.5	0.352	2.32
35° (PO)	10.3	0.336	2.19
$F_N = 0.32$			
δ [deg]	$\sigma_{K_{Trad}}$ %	K_{Trad}^{T0} %	K_{Trad}^{R}
15° (TR)	6.80	0.273	1.69
25° (TR)	5.09	0.340	2.14
35° (TR)	4.90	0.333	2.17
15° (PO)	2.50	0.248	1.54
25° (PO)	2.45	0.332	2.10
35° (PO)	0.50	0.329	2.14
$F_N = 0.35$			
δ [deg]	$\sigma_{K_{Trad}}$ %	K_{Trad}^{T0} %	K_{Trad}^{R}
35° (TR)	6.62	0.324	0.324
35° (PO)	4.38	0.321	0.321

Table 8: Modulus of the radial force on the external shaft. Turning circle

$F_N = 0.26$				
δ [deg]	$\sigma_{K_{Ty}}$ %	$\sigma_{K_{Tz}}$ %	K_{Ty}	K_{Tz}
10° (TR)	23.9 (8.1)	8.9 (6.28)	-0.062 (-0.052)	0.226 (0.227)
20° (TR)	17.1 (22.1)	7.46 (10.4)	-0.167 (-0.180)	0.276 (0.268)
35° (TR)	18.7 (16.5)	12.05 (11.8)	-0.205 (-0.225)	0.21 (0.233)
10° (PO)	–	16.5 (26.4)	–	0.205 (0.234)
20° (PO)	–	8.9 (6.4)	–	0.269 (0.278)
35° (PO)	–	9.4 (4.2)	–	0.241 (0.253)
$F_N = 0.32$				
δ [deg]	$\sigma_{K_{Ty}}$ %	$\sigma_{K_{Tz}}$ %	K_{Ty}	K_{Tz}
10° (TR)	22.7 (19.3)	4.4 (4.0)	-0.08 (-0.074)	0.242 (0.243)
20° (TR)	6.8 (9.5)	2.9 (5.76)	-0.165 (-0.169)	0.266 (0.28)
35° (TR)	6.57 (3.56)	6.58 (2.8)	-0.178 (-0.189)	0.223 (0.233)
10° (PO)	–	3.2 (6.7)	–	0.238 (0.239)
20° (PO)	–	2.13 (2.23)	–	0.267 (0.27)
35° (PO)	–	5.9 (6.3)	–	0.253 (0.257)
$F_N = 0.35$				
δ [deg]	$\sigma_{K_{Ty}}$ %	$\sigma_{K_{Tz}}$ %	K_{Ty}	K_{Tz}
20° (TR)	5.3 (3.0)	2.2 (2.89)	-0.178 (-0.151)	0.224 (0.24)
35° (TR)	4.5 (2.2)	2.97 (2.2)	-0.142 (-0.192)	0.239 (0.238)
20° (PO)	–	3.1 (5.4)	–	0.237 (0.242)
35° (PO)	–	3.1 (4.9)	–	0.236 (0.251)

Table 9: Bearing forces on the internal shaft; zig–zag maneuver (in brackets the mean value of the 1^{st} overshoot phase)

$F_N = 0.26$				
δ [deg]	$\sigma_{K_{Ty}}$ %	$\sigma_{K_{Tz}}$ %	$K_{Ty} ratio$	K_{Tz}
10°	6.5 (0.3)	41.7 (38.2)	0.251 (0.237)	0.021 (0.03)
20°	4.38 (3.9)	45.5 (50.5)	30.8 (0.293)	-0.019 (-0.013)
35°	9.7 (8.6)	20.8 (17.4)	0.338 (0.343)	-0.081 (-0.093)
$F_N = 0.32$				
δ [deg]	$\sigma_{K_{Ty}}$ %	$\sigma_{K_{Tz}}$ %	$K_{Ty} ratio$	K_{Tz}
10°	10.4 (2.9)	11.39 (6.4)	0.188 (0.162)	0.114 (0.118)
20°	5.8 (1.2)	50.5 (40.5)	0.305 (0.274)	0.018 (0.033)
35°	6.2 (3.5)	37.3 (38.9)	0.338 (0.347)	-0.042 (-0.035)
$F_N = 0.35$				
δ [deg]	$\sigma_{K_{Ty}}$ %	$\sigma_{K_{Tz}}$ %	$K_{Ty} ratio$	K_{Tz}
20°	4.1 (0.8)	45.6 (20.9)	0.262 (0.25)	0.023 (0.03)
35°	2.5 (0.9)	22 (26.5)	0.321 (0.313)	-0.036 (-0.026)

Table 10: Bearing forces on the external shaft; zig–zag maneuver (in brackets the mean value of the 1^{st} overshoot phase)

$F_N = 0.26$			
δ [deg]	$\sigma_{K_{Trad}}$ %	K_{Trad}^{T0} %	K_{Trad}^{R}
10° (TR)	10.3 (6.2)	0.22 (0.22)	1.51 (1.58)
20° (TR)	7.4 (11.7)	0.30 (0.29)	2.00 (2.01)
35° (TR)	13.6 (10.9)	0.237 (0.276)	1.57 (1.73)
10° (PO)	17.1 (25.0)	0.2 (0.232)	1.37 (1.51)
20° (PO)	7.2 (10.4)	0.29 (0.305)	1.94 (1.91)
35° (PO)	9.2 (5.5)	0.251 (0.269)	1.67 (1.77)
$F_N = 0.32$			
δ [deg]	$\sigma_{K_{Trad}}$ %	K_{Trad}^{T0} %	K_{Trad}^{R}
10° (TR)	6.4 (4.7)	0.247 (0.249)	1.50 (1.51)
20° (TR)	4.46 (6.4)	0.293 (0.308)	1.73 (1.77)
35° (TR)	7.03 (5.9)	0.245 (0.256)	1.49 (1.56)
10° (PO)	4.2 (8.4)	0.243 (0.241)	1.47 (1.46)
20° (PO)	4.1 (1.0)	0.290 (0.287)	1.72 (1.65)
35° (PO)	4.99 (6.0)	0.261 (0.261)	1.59 (1.58)
$F_N = 0.35$			
δ [deg]	$\sigma_{K_{Trad}}$ %	K_{Trad}^{T0} %	K_{Trad}^{R}
20° (TR)	3.8 (2.3)	0.262 (0.276)	1.62 (1.70)
35° (TR)	8.0 (3.0)	0.242 (0.264)	1.46 (1.55)
20° (PO)	4.1 (4.5)	0.250 (0.263)	1.54 (1.62)
35° (PO)	3.1 (5.0)	0.249 (0.263)	1.51 (1.48)

Table 11: Modulus of the radial force on the internal shaft; zig–zag maneuver (in brackets the mean value of the 1^{st} overshoot phase)

$F_N = 0.26$			
δ [deg]	$\sigma_{K_{Trad}}$ %	K_{Trad}^{T0} %	K_{Trad}^{R}
10°	5.9 (1.0)	0.254 (0.242)	1.74 (1.66)
20°	4.2 (3.6)	0.30 (0.28)	2.05 (1.97)
35°	10 (9.6)	0.339 (0.346)	2.28 (2.39)
$F_N = 0.32$			
δ [deg]	$\sigma_{K_{Trad}}$ %	K_{Trad}^{T0} %	K_{Trad}^{R}
10°	5.1 (1.8)	0.225 (0.21)	1.36 (1.27)
20°	5.9 (1.2)	0.304 (0.274)	1.81 (1.68)
35°	4.8 (3.4)	0.348 (0.346)	2.13 (2.13)
$F_N = 0.35$			
δ [deg]	$\sigma_{K_{Trad}}$ %	K_{Trad}^{T0} %	K_{Trad}^{R}
20°	3.4 (0.5)	0.26 (0.252)	1.62 (1.56)
35°	2.8 (1.1)	0.32 (0.31)	1.95 (1.95)

Table 12: Modulus of the radial force on the external shaft; zig–zag maneuver (in brackets the mean value of the 1^{st} overshoot phase)

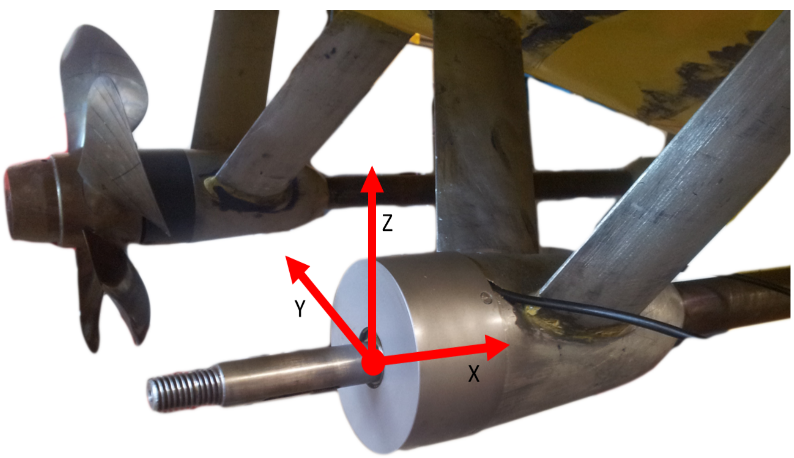

Figure 1: Layout of the shaft with the bi–axial transducer

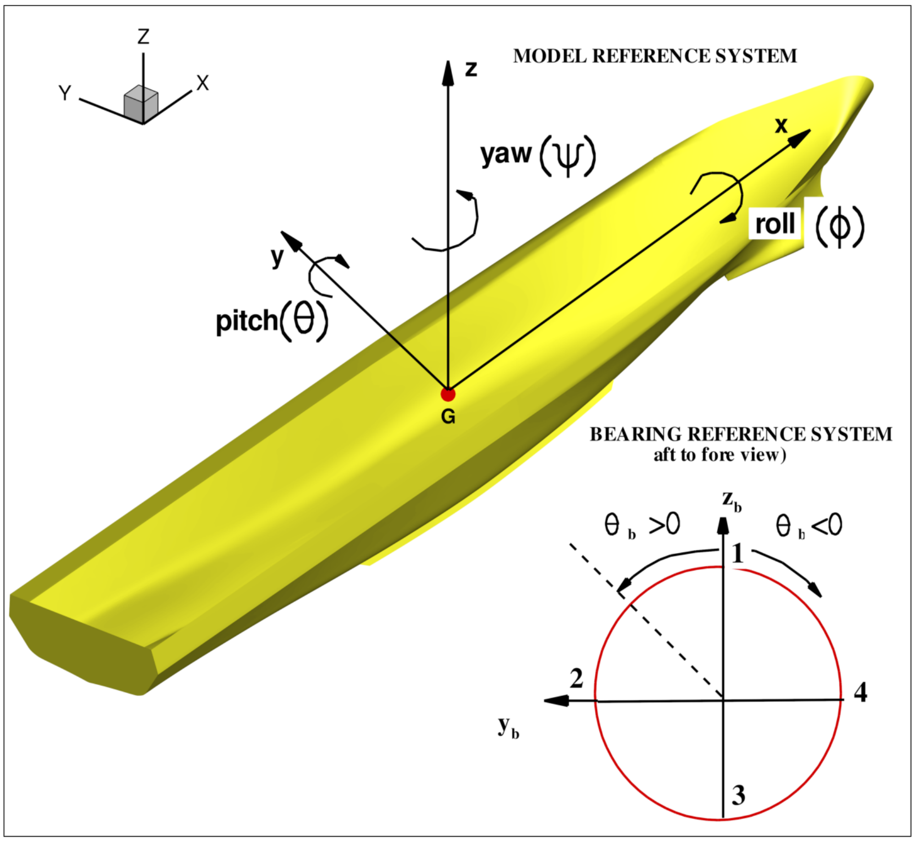

Figure 2: Reference system

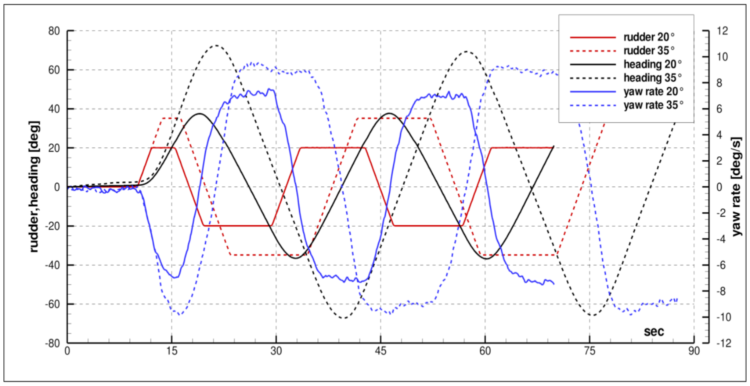

(a) heading, rudder and yaw rate

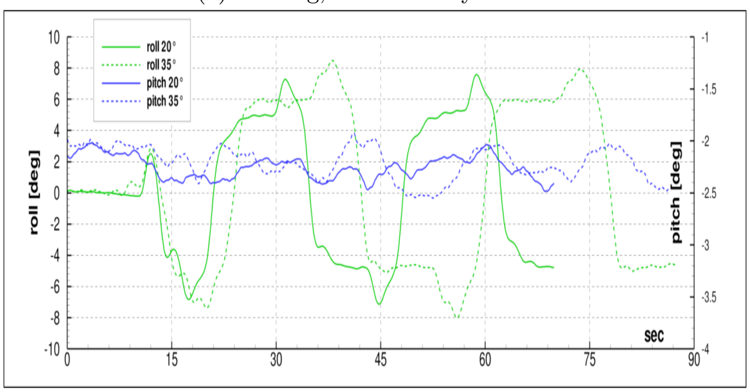

(b) roll and pitch angles

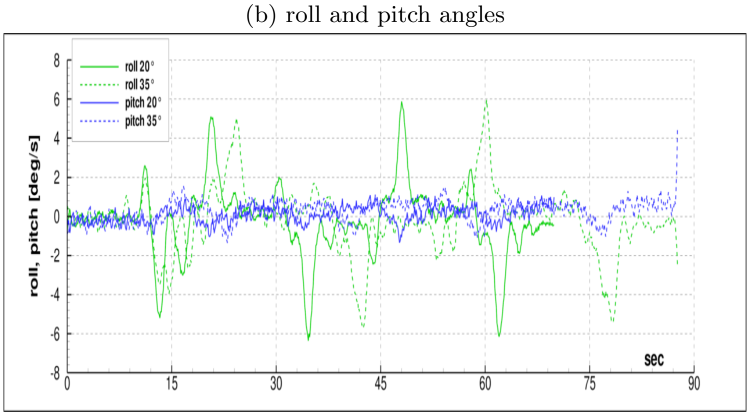

(c) roll and pitch rate

Figure 3: Dynamic response during ±20° and ±35° zig–zag tests; $F_N = 0.32$

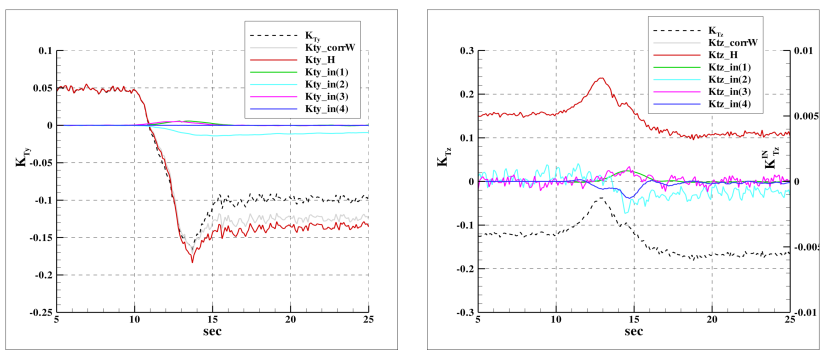

(a) K_{TY}

(b) K_{TZ}

Figure 4: Contribution of inertial and measured loads. Internal shaft

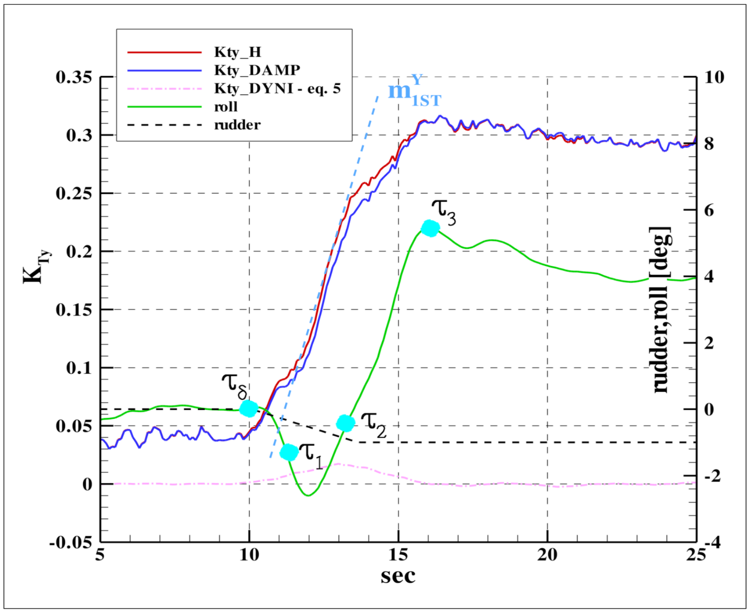

(a) K_{TY}

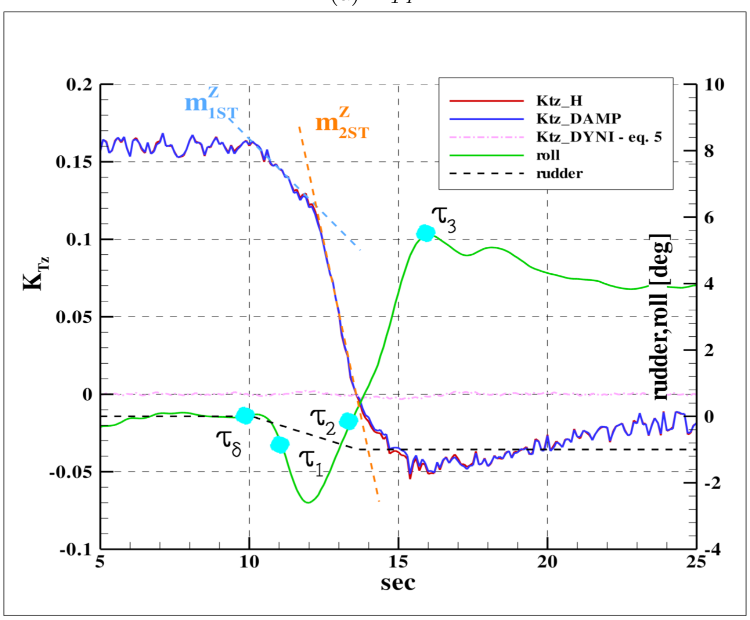

(b) K_{TZ}

Figure 5: Time hystories of K_{TY} and K_{TZ}; transient at the start of the turn. External propeller

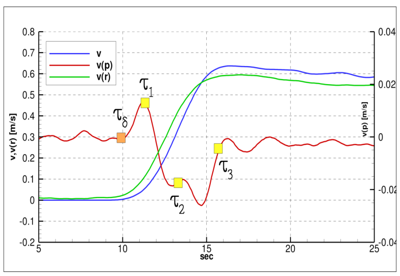

(a) lateral velocities

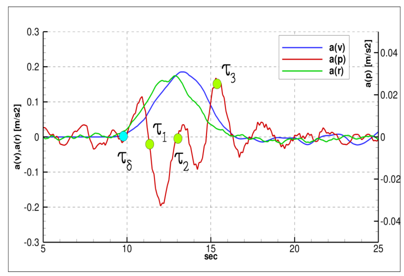

(b) lateral accelerations

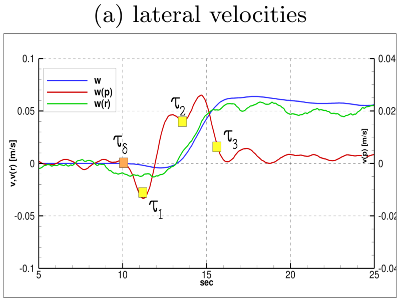

(c) vertical velocities

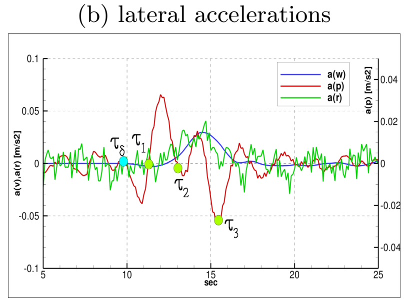

(d) vertical accelerations

Figure 6: Reconstruction of the dynamics of the propeller. Velocity and accelerations expressed relative to the propeller

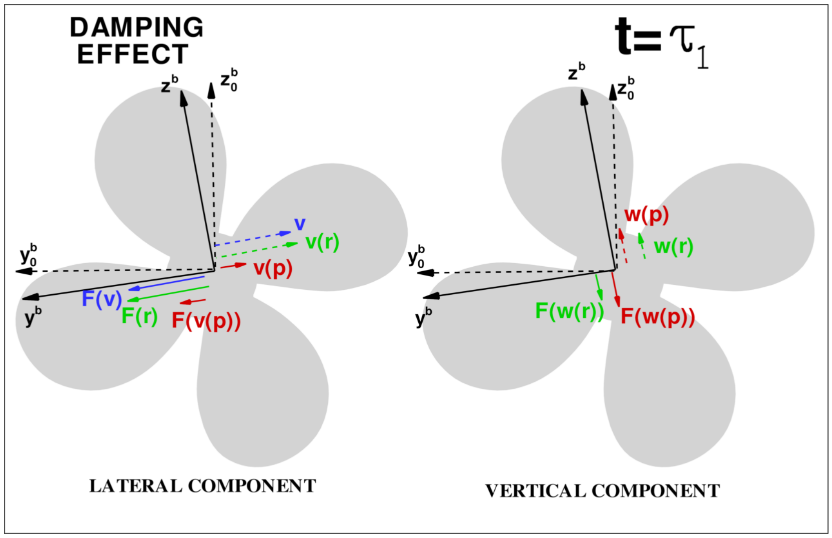

(a) velocities

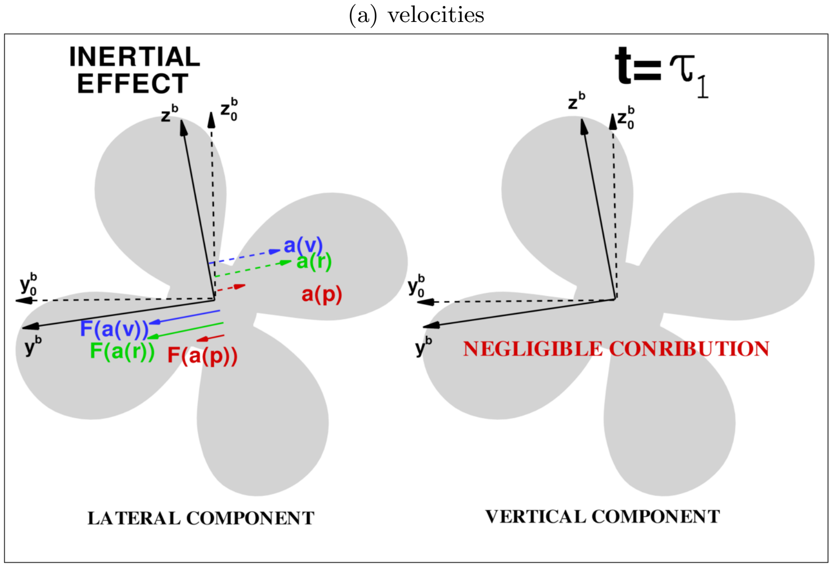

(b) accelerations

Figure 7: Correlation between the motion induced velocities and the hydrodynamic loads; $t = \tau_1$

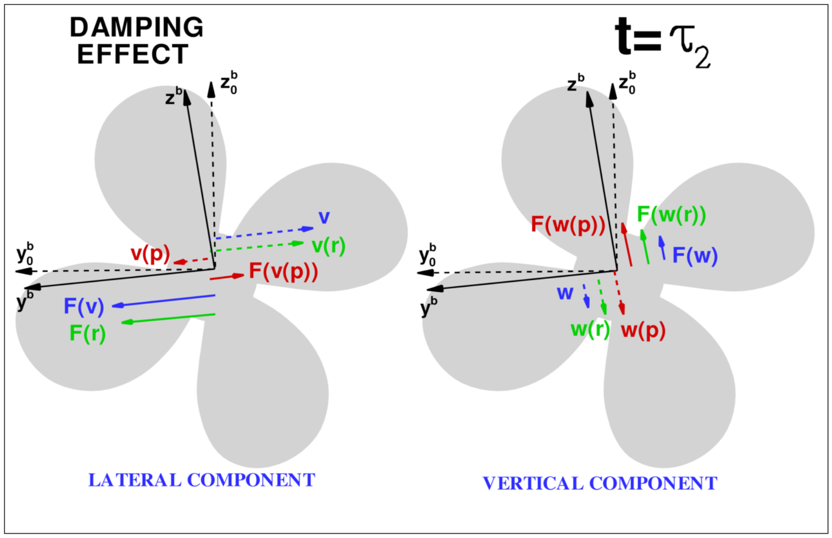

(a) velocities

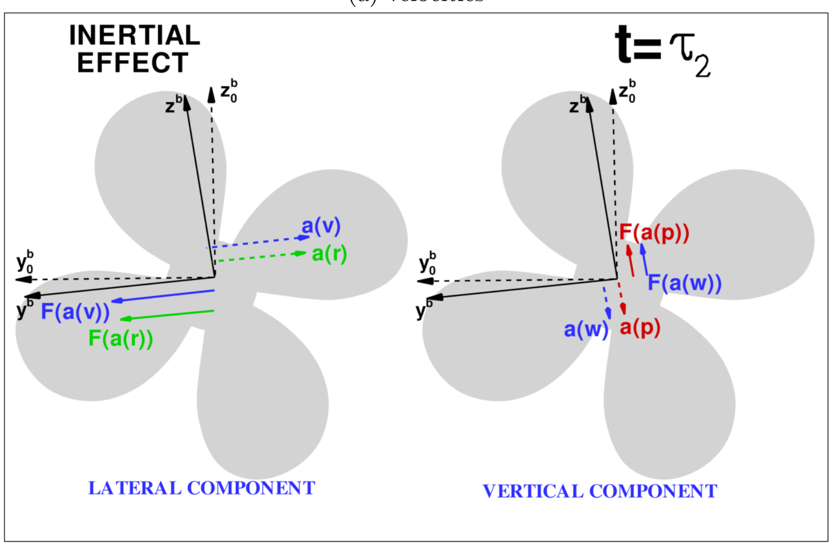

(b) accelerations

Figure 8: Correlation between the motion induced velocities and the hydrodynamic loads; $t = \tau_2$

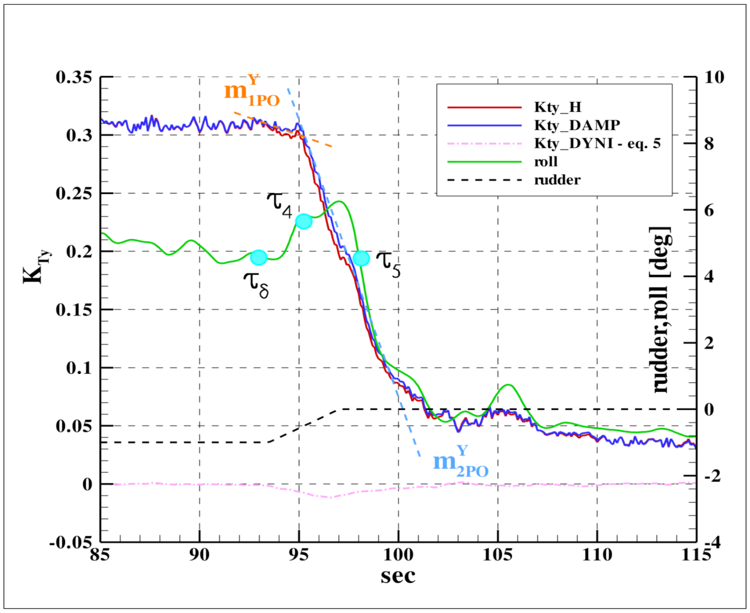

(a) K_{TY}

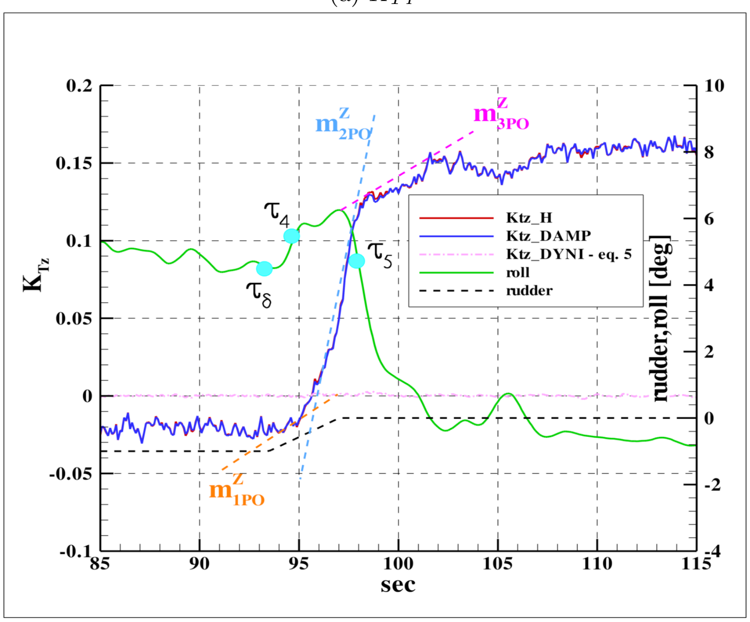

(b) K_{TZ}

Figure 9: Time histories of K_{TY} and K_{TZ}; transient at the pull–out. External propeller

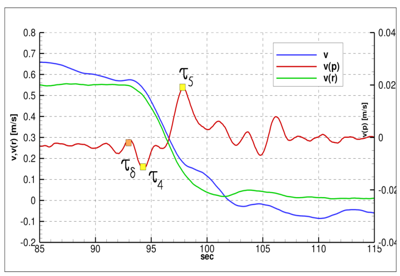

(a) velocities

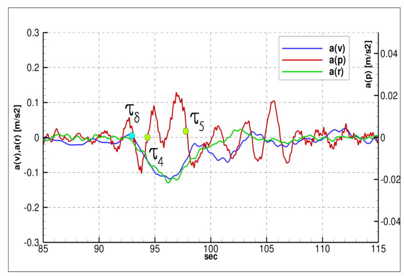

(b) accelerations

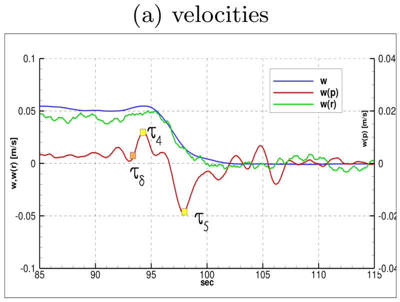

(c) velocities

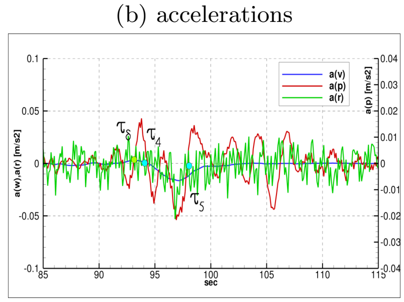

(d) accelerations

Figure 10: Reconstruction of the dynamics of the propeller. Velocity and accelerations expressed relative to the propeller

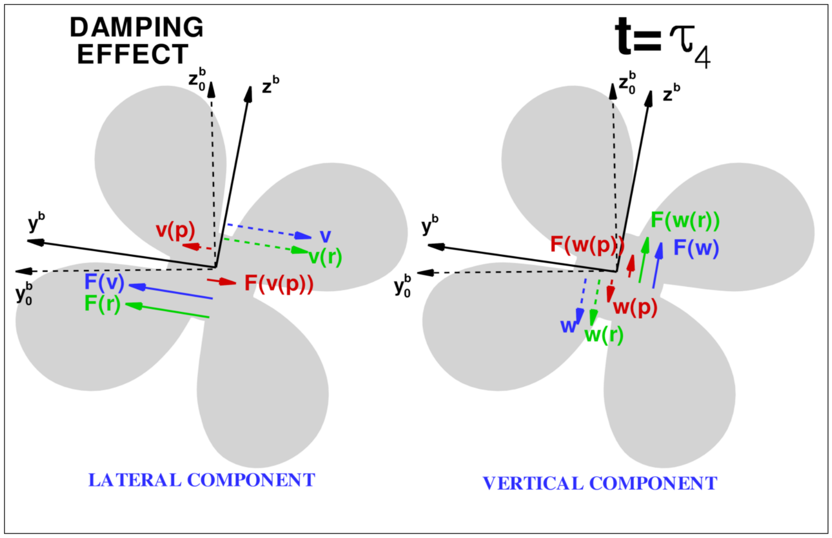

(a) lateral velocities

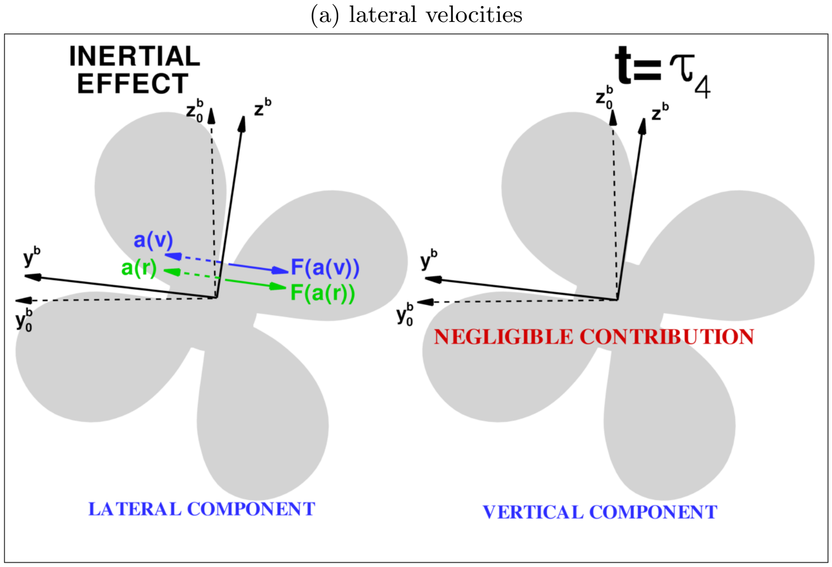

(b) lateral accelerations

Figure 11: Correlation between the motion induced velocities and the hydrodynamic loads; $t = \tau_4$

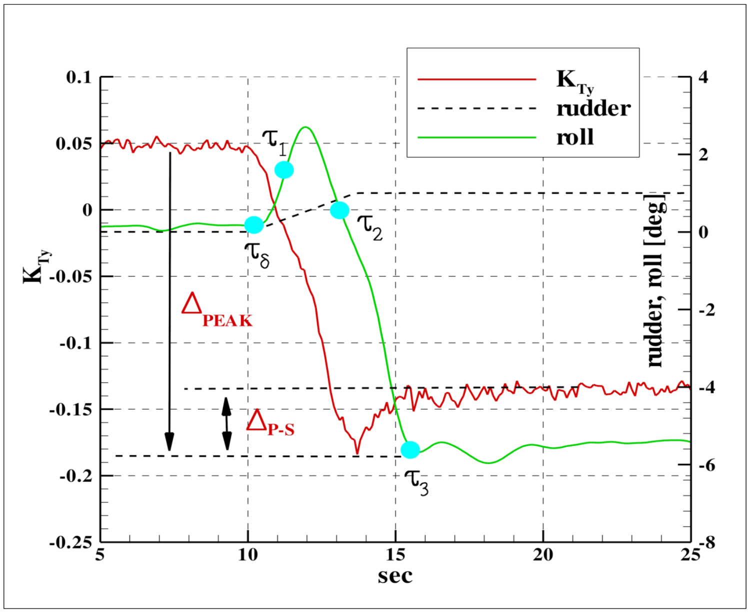

(a) K_{TY}

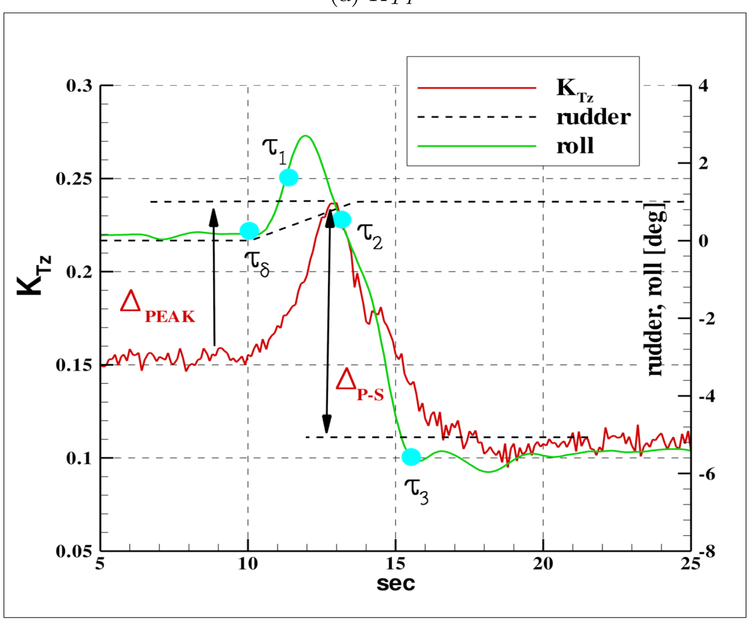

(b) K_{TZ}

Figure 12: Time histories of K_{TY} and K_{TZ}; transient at the start of the turn. Internal propeller

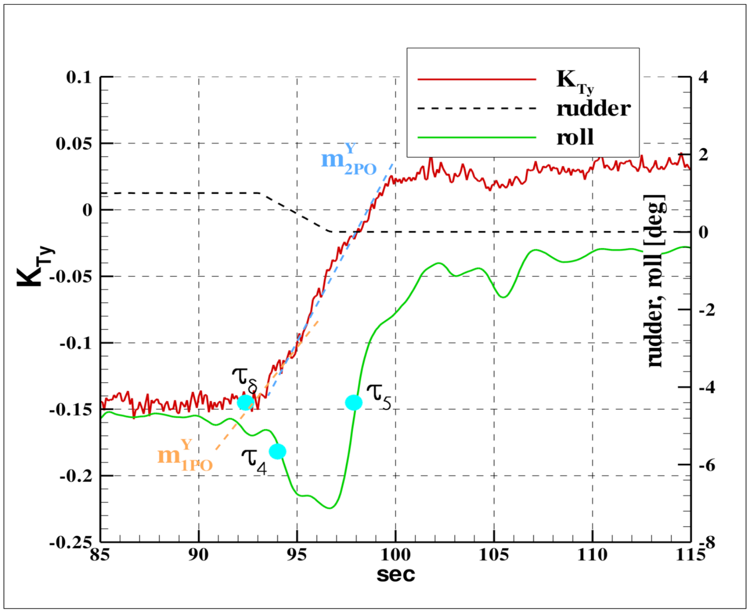

(a) K_{TY}

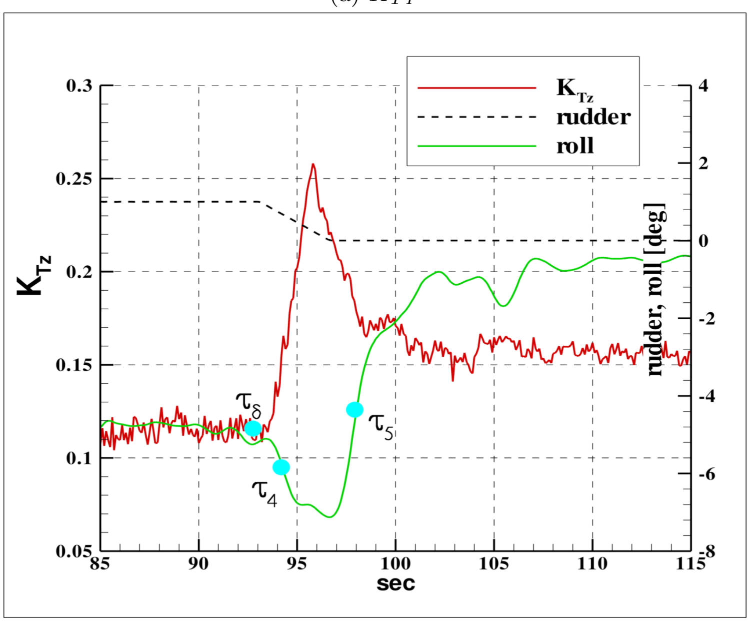

(b) K_{TZ}

Figure 13: Time histories of K_{TY} and K_{TZ}; transient at the pull–out. Internal propeller

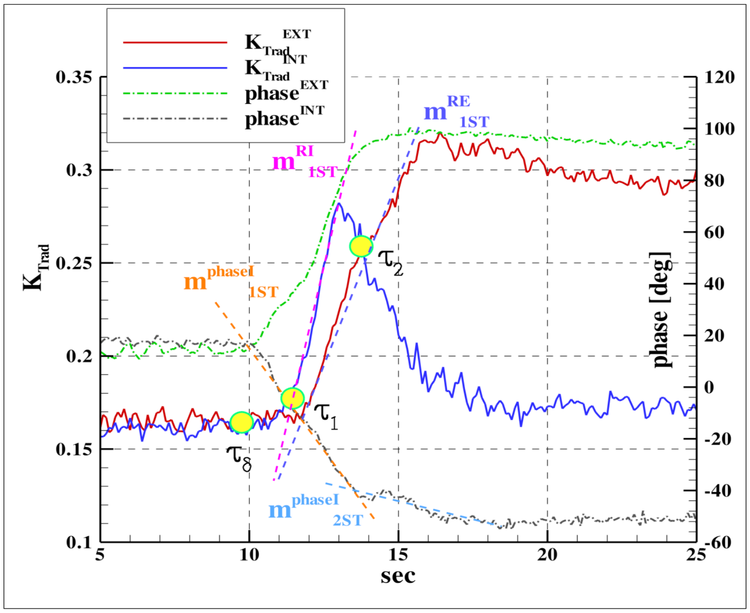

(a) Start of the turn

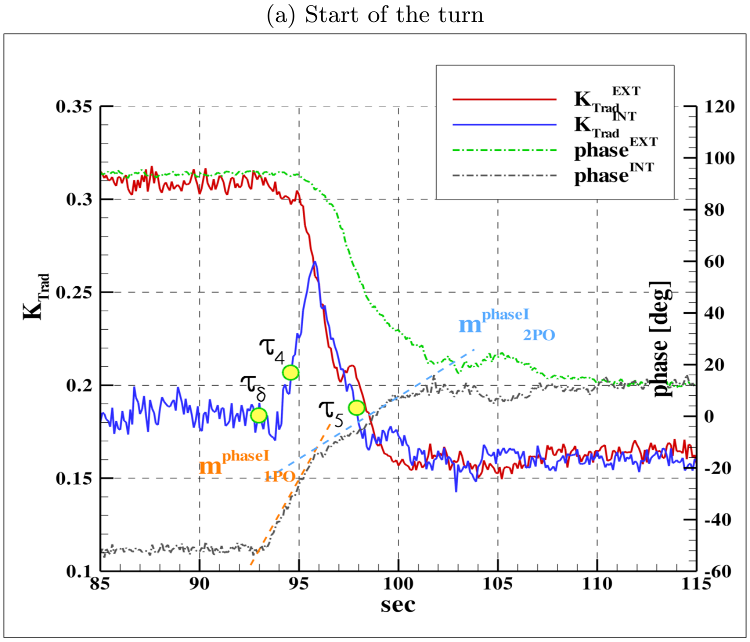

(b) Pull–out

Figure 14: Evolution of the radial bearing force and phase angle during transients

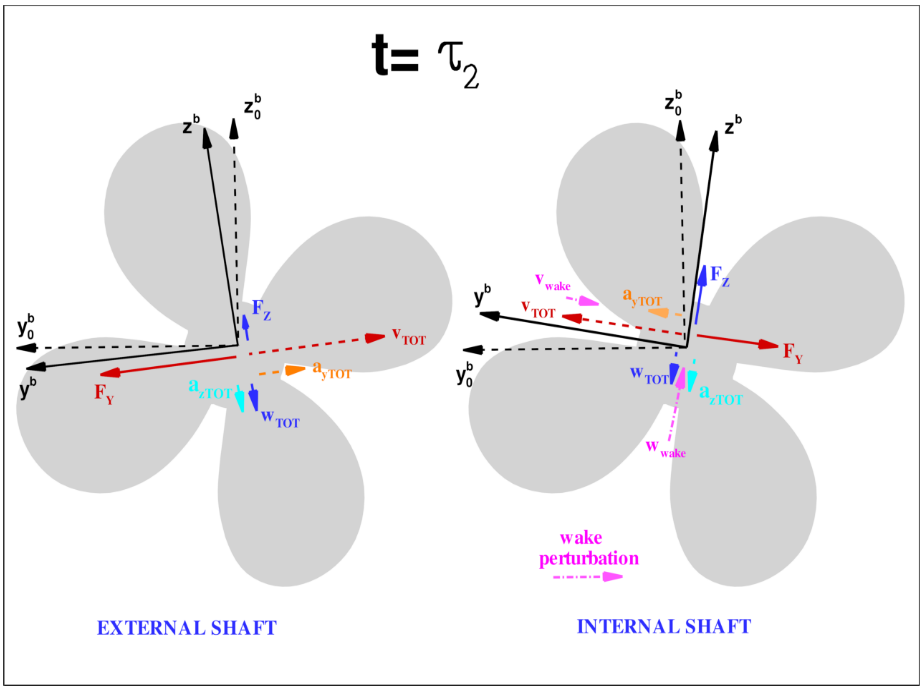

Figure 15: Synthesis of the phenomenology related to generation of the propeller radial force; external and internal propeller

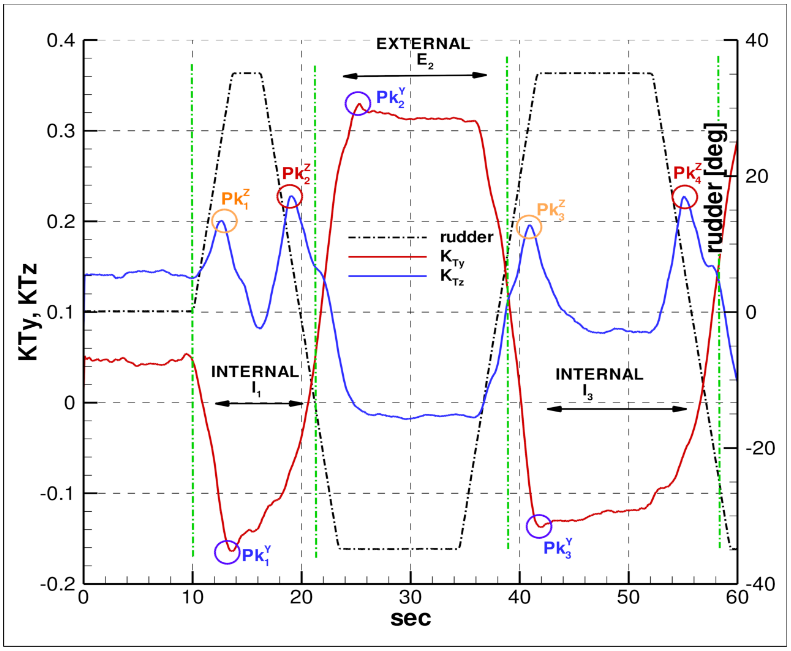

(a) lateral and vertical components

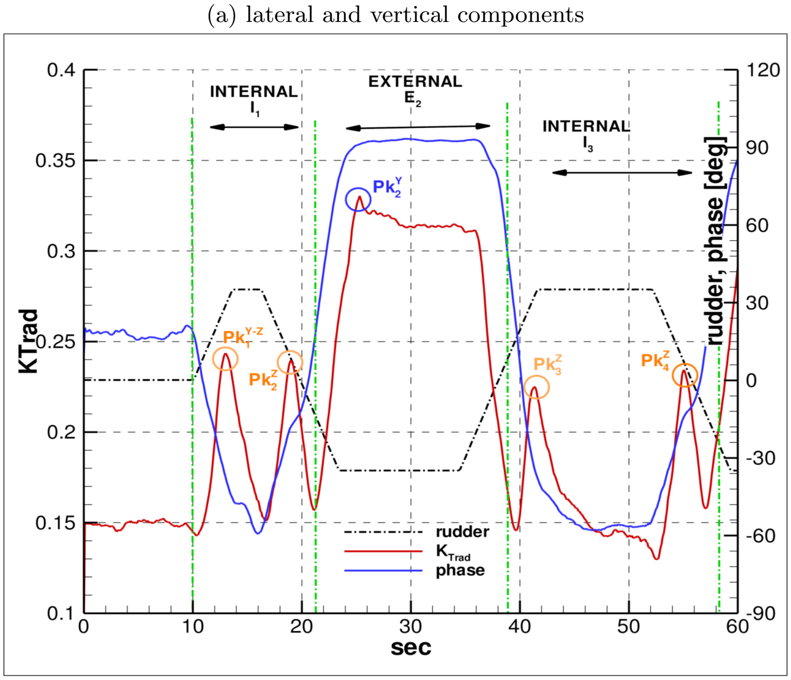

(b) radial force and phase angle

Figure 16: Radial loads and phase angle; zig–zag ±35°

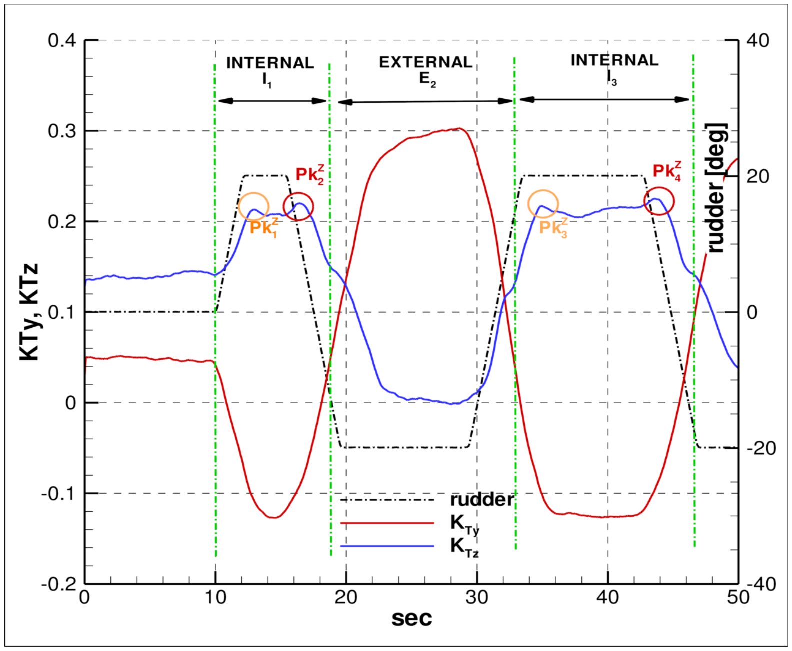

(a) lateral and vertical components

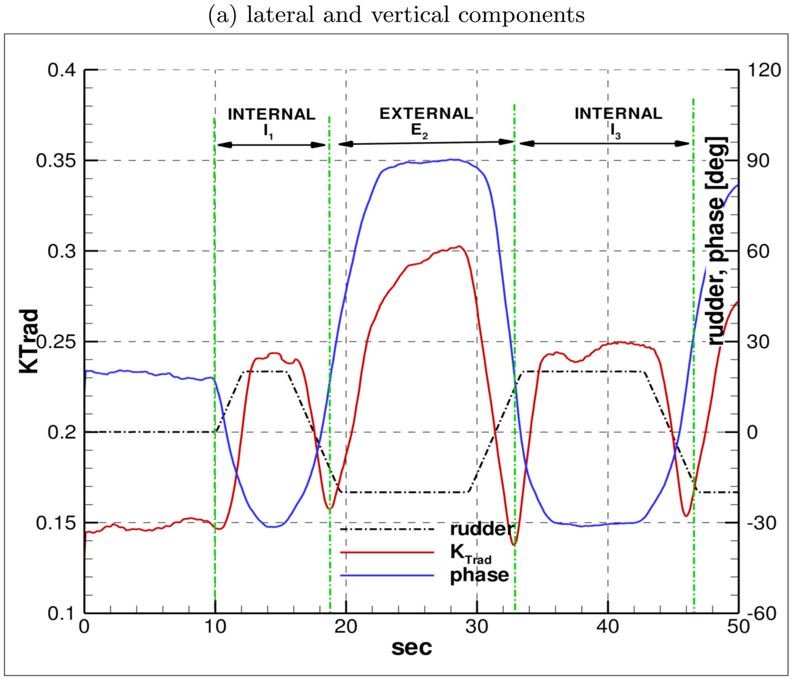

(b) radial force and phase angle

Figure 17: Radial loads and phase angle; zig–zag $\pm 20^\circ$

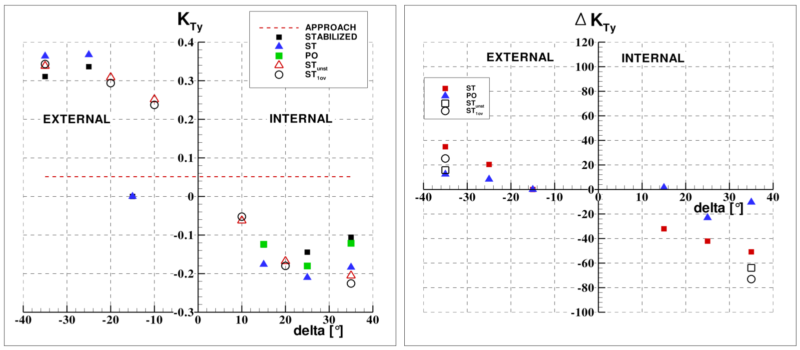

(a) F_N=0.26

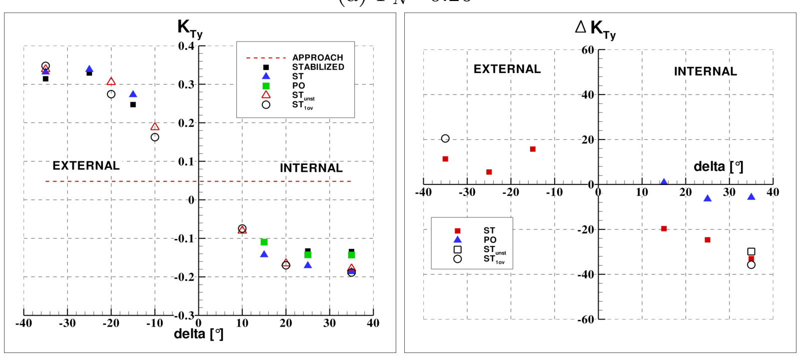

(b) F_N=0.32

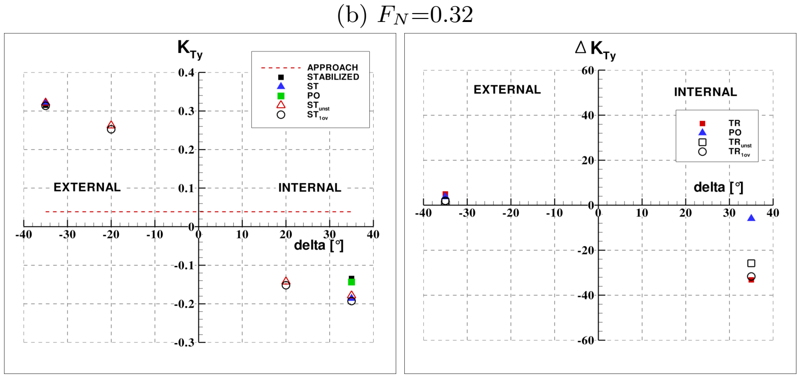

(c) F_N=0.35

Figure 18: Systematic analysis of the horizontal force

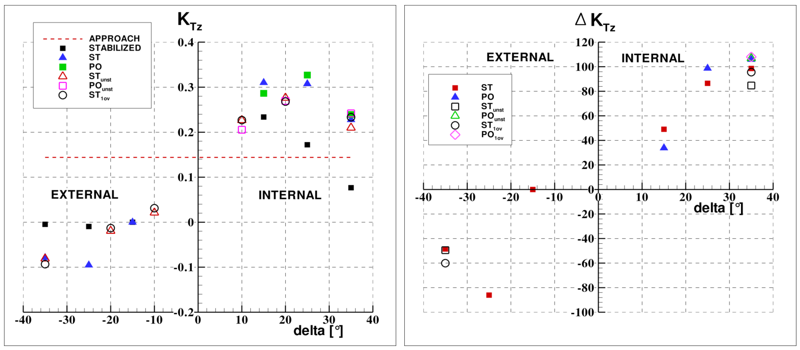

(a) F_N=0.26

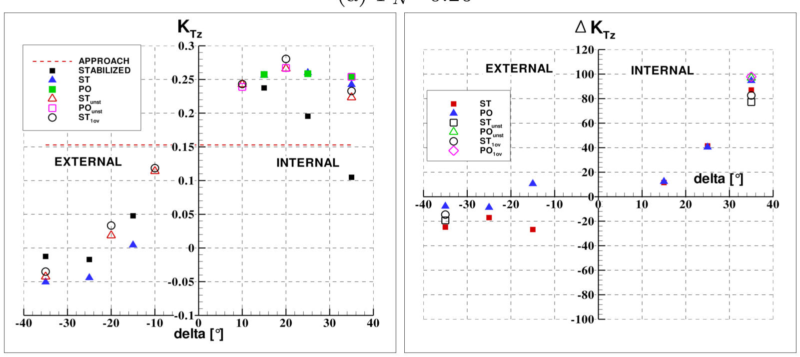

(b) F_N=0.32

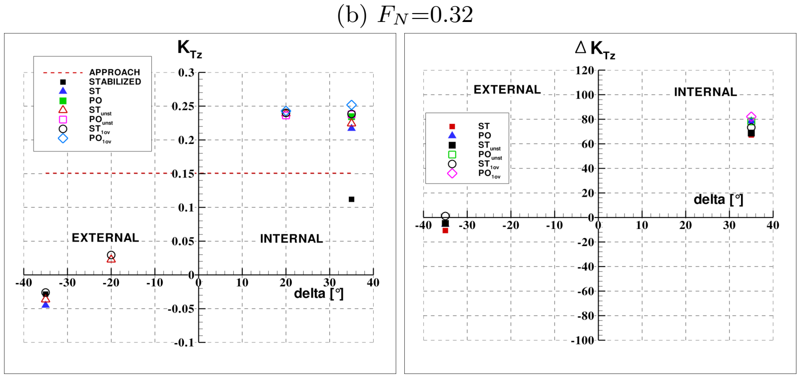

(c) F_N=0.35

Figure 19: Systematic analysis of the vertical force

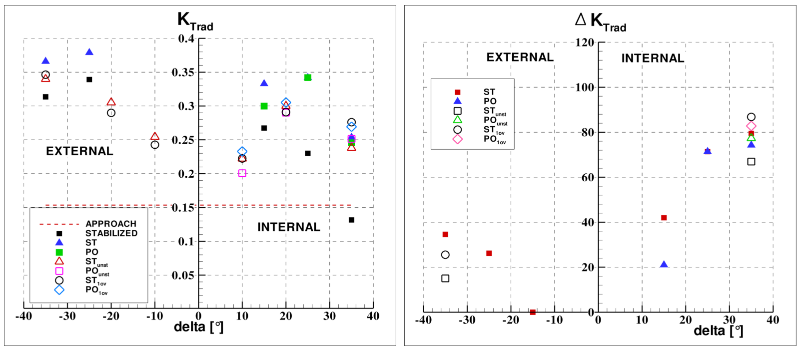

(a) F_N=0.26

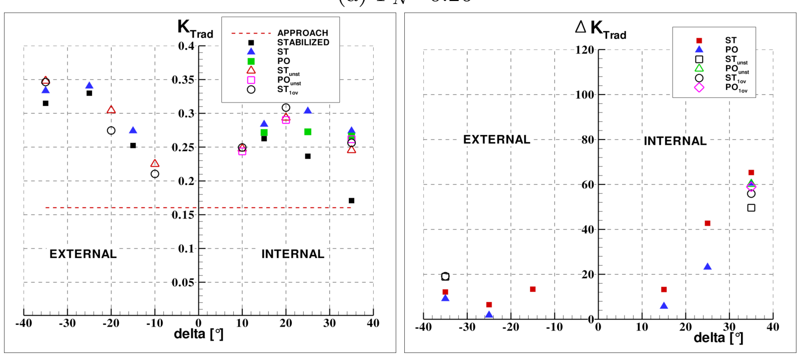

(b) F_N=0.32

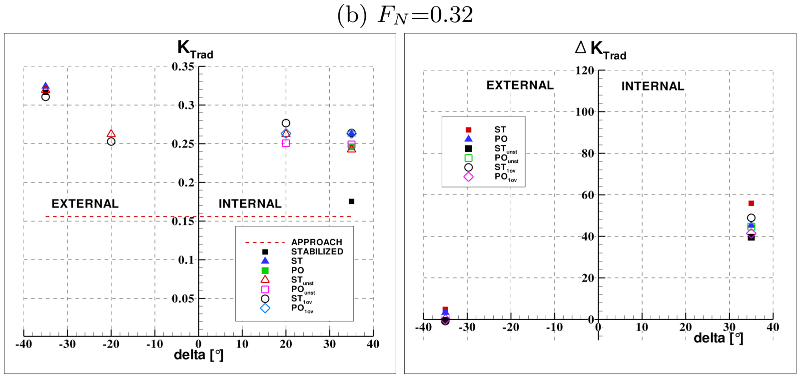

(c) F_N=0.35

Figure 20: Systematic analysis of the radial force

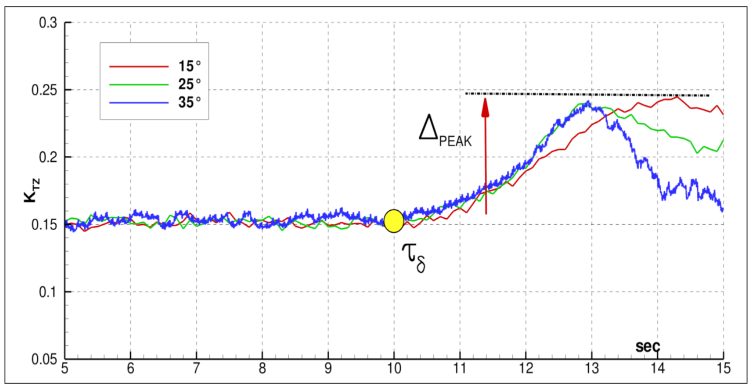

(a) Start of turning

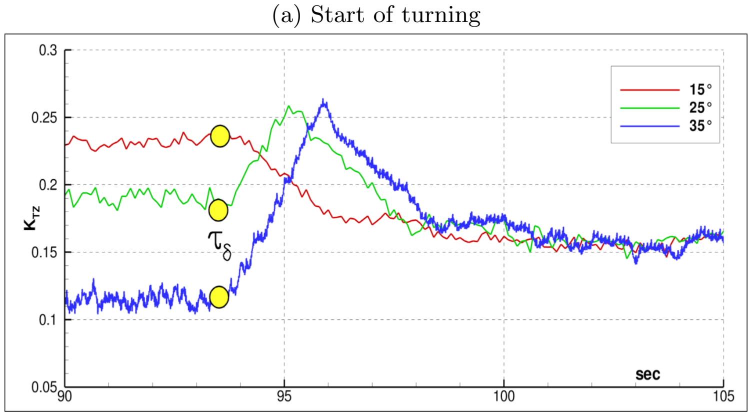

(b) Pull–out

Figure 21: Increase of K_{TZ} on the internal shaft in relation to the different rudder angles

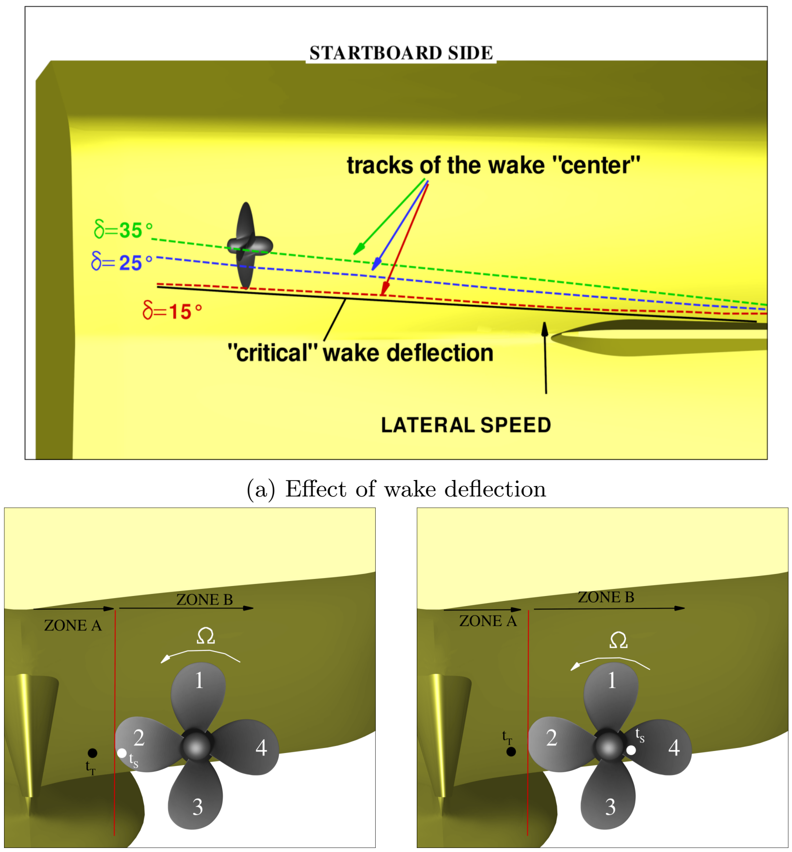

(a) Effect of wake deflection

(b) wake evolution at $\delta = 15°$

(c) wake evolution at $\delta = 35°$

Figure 22: Schematic representation of the propeller–wake interaction